ACS Catalysis

pubs.acs.org/acscatalysis

Research Article

Ruthenium Nanoparticles on Water-Stable Supported Ionic Liquid Phases as Catalytic Systems for Aqueous Phase CO_2 Hydrogenation

Neha Antil, Savarithai Jenani Louis Anandaraj, Liqun Kang, Hooman Ghazi Zahedi, Serena DeBeer, Walter Leitner,* and Alexis Bordet*

Cite This: *ACS Catal.* 2025, 15, 14601−14610

Read Online

ACCESS | Metrics & More | Article Recommendations | Supporting Information

ABSTRACT: The first example of a hydrothermally stable Supported Ionic Liquid Phase (SILP) material was designed and used successfully as a support for ruthenium nanoparticles (Ru NPs) in catalytic hydrogenation of CO_2 to formic acid in water/amine media. Imidazolium-based ionic liquids (ILs) were grafted on activated carbon (AC) through the formation of robust carbon−carbon bonds via diazotization, followed by deposition of Ru NPs using an organometallic approach. Compared to reference materials, the presence of the IL on the solid material led not only to improved catalyst performance of the nanoparticles but also to higher formic acid concentrations in the reaction mixture due to additional thermodynamic stabilization of the product. The Ru@$SILP_{AC}$ catalysts showed high activity (turnover frequencies (TOFs) exceeding 3000 h^{-1}), productivity (turnover numbers (TONs) up to 15,000 in a single batch), and stability (10 recycling with no apparent loss of activity). These results define a new benchmark for NP-based catalysts in CO_2 hydrogenation to formic acid and suggest promising potential for the application of such NP@SILP materials in aqueous phase hydrogenation reactions in general.

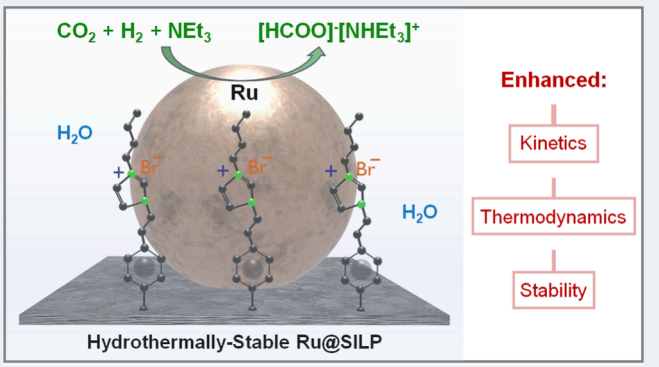

KEYWORDS: *supported ionic liquid phases, nanoparticles, CO_2 hydrogenation, aqueous phase catalysis, thermodynamics*

INTRODUCTION

The catalytic conversion of CO_2 into valuable products is a central pillar of approaches to reduce our dependence on fossil resources and potentially mitigate the effects of climate change.[1−5] Research efforts on the reduction of CO_2 using molecular hydrogen (H_2) from nonfossil sources are intensively focusing on its conversion into energy carriers and chemicals such as methanol, formic acid, and hydrocarbons.[6−13] The hydrogenation of CO_2 to formic acid has garnered particular interest due to existing applications of this molecule as well as future perspectives as C_1 feedstock and a potential platform for chemical energy storage.[14−18] While numerous homogeneous catalysts have been developed,[19−21] there are comparably few metal nanoparticles (NPs)-based materials acting as catalysts for this reaction, and their performance remains as yet modest.[22−24] A promising approach consists of using colloidal dispersions of NPs in ionic liquids (ILs), whereby interactions between NPs and ILs were found to improve stability and activity of NPs while providing opportunities for selectivity tuning.[25−29] For example, Dupont and co-workers reported the use of bimetallic FeRu NPs in various imidazolium-based IL media for the hydrogenation of CO_2 to CO and formic acid.[26] The structure of the ILs allowed shifting the selectivity of NPs toward CO or formic acid while also improving their activity. Furthermore, the presence of ILs was found to be beneficial for the stabilization of formic acid when used as cosolvents in dimethyl sulfoxide (DMSO). The incorporation of ionic liquids, whether as solvents, cosolvents, or additives, has been shown to significantly enhance the efficiency of CO_2 hydrogenation processes.[30−33] In this context, the immobilization of NPs and ILs on a single support material is highly desirable to enhance the productivity per metal used, minimize the amount of IL used, and enable recyclability.[34−38] However, the concepts derived from studies of NPs dispersed in the liquid phase may not be directly applicable to supported systems because NPs/support matrix interactions often become dominating control factors.[39,40] In addition, NPs@SILPs are until now poorly stable under aqueous conditions,[41] which is, however, a preferred reaction medium for CO_2 hydrogenation due to its use in CO_2 scrubbing technologies[42−44] and its ability to stabilize the product of this otherwise thermodynamically unfavorable reaction.[14,45−47]

Received: May 27, 2025
Revised: August 1, 2025
Accepted: August 4, 2025

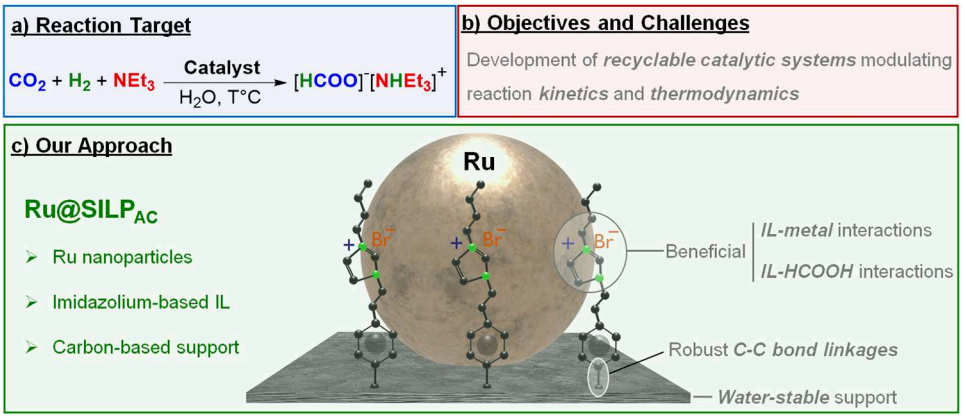

Figure 1. Illustration of the general approach of this study with (a) the target reaction, (b) key objectives and challenges, and (c) our catalyst design strategy.

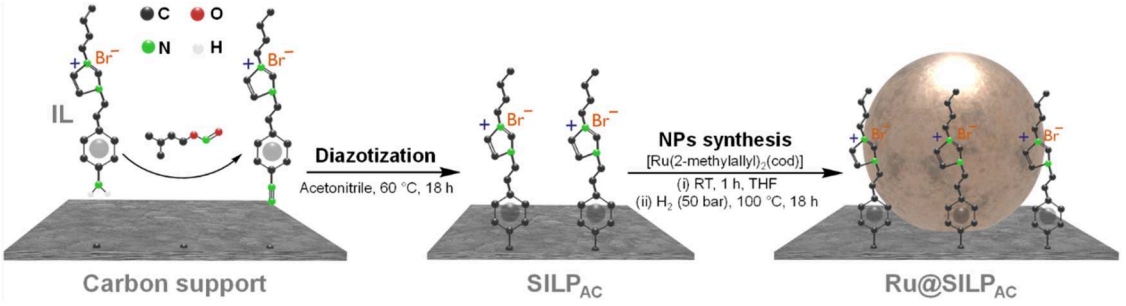

Figure 2. Reaction scheme for the preparation of $SILP_{AC}$ and $Ru@SILP_{AC}$.

Thus, we set our first goal in this study to develop supported ionic liquid phase (SILP) support materials that are stable in water and aqueous amine solutions at elevated temperatures and H_2 pressures. As a result, we report the design and synthesis of a new generation of carbon-based imidazolium-based SILPs, specifically engineered to be hydrothermally stable and thus to overcome the limitations of typical SILP designs relying on chemisorption by silanization, esterification, or amidation (Figure 1). Ru NPs were immobilized on this novel matrix and on reference materials to investigate the influence of NP−IL interactions on catalytic activity (kinetics) and productivity (stability) as well as on the stabilization of formic acid in the reaction mixture (thermodynamics) in the hydrogenation of CO_2 to formic acid in water and aqueous amine solutions.

RESULTS AND DISCUSSION

Material Synthesis and Characterization. The new aniline-functionalized imidazole-based ionic liquid ([3-(4-aminophenethyl)-1-butyl-1*H*-imidazol-3-ium]bromide, noted IL) was synthesized by adapting existing procedures[34,41] (see Scheme S1 and Supporting Information for detailed synthetic procedure and characterization). The covalent attachment of IL to the surface of activated carbon (AC) was achieved by diazotization to form robust C−C bonds (Figure 2). In brief, the adapted literature procedure[42,43] involved the addition of isoamyl nitrite to suspensions of IL (3 mmol) and AC (1 g) in acetonitrile, followed by stirring the resulting mixture in the dark at 60 °C for 18 h. The diazonium salt was generated in situ and used directly, obviating safety concerns associated with its isolation. The use of well-dried AC (high vacuum overnight) and protection of the reaction mixture from light were found to be critical to the success of the reaction. The resulting black powder was thoroughly washed with acetonitrile and water to remove any nongrafted IL molecules.

IL content in the washing phase was quantified by ^{1}H NMR and used to determine the IL loading on AC (2.2 $mmol_{IL}·g^{-1}$, 73%, see Table S1). Interestingly, this synthetic approach can be applied flexibly to other carbon-based support materials (Table S1). The tunability, reproducibility, and scalability of this synthetic approach to $SILP_{AC}$ were demonstrated over a range of IL loadings (0.55−2.4 $mmol_{IL}·g^{-1}$, Table S2), $SILP_{AC}$ batches (Table S3), AC batches (Table S4), and reaction scale (0.1−2 g of support material, Table S5), with variations in IL loading typically below 10%.

Characterization of $SILP_{AC}$ by Fourier transform infrared spectroscopy (FT-IR) exhibited bands characteristic of IL, such as C−H stretching vibrations of the imidazole ring at 2987−2916 cm^{-1} and C−N stretching at 1157 cm^{-1} (Figure S1).[48,49] Thermogravimetric analysis (TGA) revealed that $SILP_{AC}$ is thermally stable up to 250 °C (Figure S2a). Thorough treatment of $SILP_{AC}$ under various conditions (e.g., H_2O at 25 °C, D_2O at 100 °C + 60 bar H_2, toluene at 25 °C) and characterization by ^{1}H NMR (Figure S3), and elemental analysis (inductively coupled plasma-optical emission spectrometry (ICP-OES) and X-ray fluorescence (XRF), Table S6) demonstrated the absence of substantial IL leaching, and thus the robustness of $SILP_{AC}$ in aqueous and organic media. This represents an important improvement over previously reported silica-, metal oxide-, and carbon-based SILPs relying on water-sensitive Si−O−Si, C−O, and C−N bonds as linkers.[36,41,50,51]

The organometallic synthesis of Ru NPs on $SILP_{AC}$ with different IL loadings (0.55−2.4 $mmol·g^{-1}$) was conducted following a method previously reported for the SiO_2-based

https://doi.org/10.1021/acscatal.5c03605
ACS Catal. 2025, 15, 14601−14610

Table 1. Characterization of Ru@AC and Ru@SILP$_{AC}$ Materials, Including N_2 Adsorption, ICP-OES, and Electron Microscopy

Ru@support	surface area ($m^2 \cdot g^{-1}$)	IL loading(mmol·g^{-1})	Ru loading(mmol·g^{-1})	NPs size(nm)	surface Ru (%)
Ru@AC	2840		0.085	1.2 ± 0.3	51.8
Ru@SILP$_{AC}$	1725	0.5	0.090	1.4 ± 0.3	45.9
Ru@SILP$_{AC}$	1149	0.8	0.077	1.3 ± 0.3	48.6
Ru@SILP$_{AC}$	1282	1.1	0.081	1.5 ± 0.3	43.4
Ru@SILP$_{AC}$	1072	1.7	0.083	1.6 ± 0.3	41.1
Ru@SILP$_{AC}$	964	2.4	0.080	1.5 ± 0.3	43.4

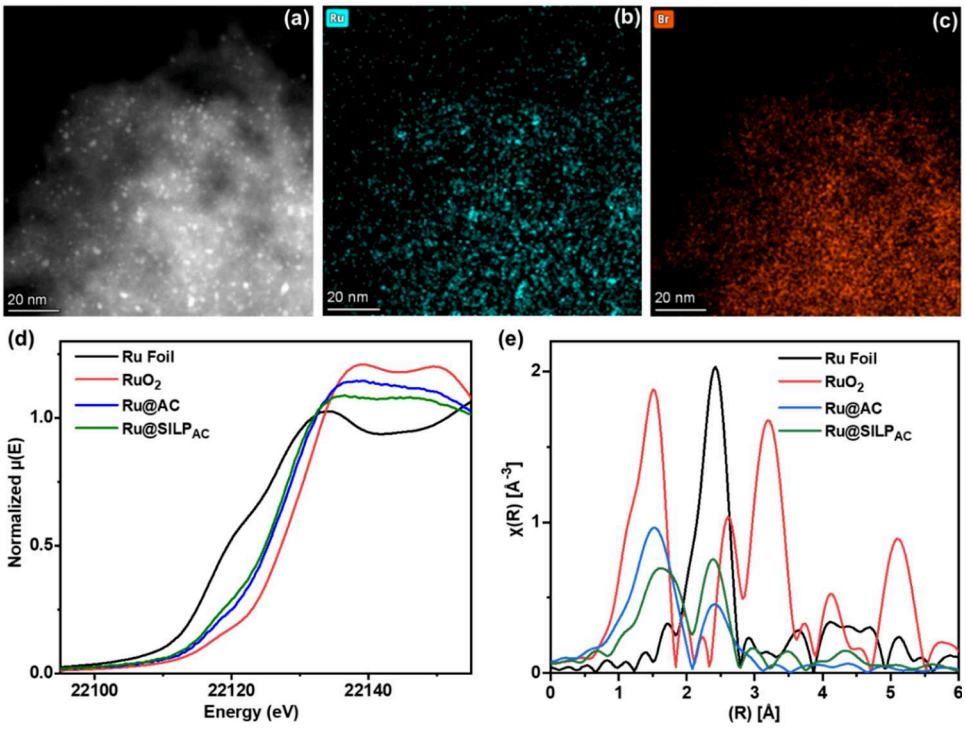

Figure 3. Characterization of Ru@SILP$_{AC}$ (1.1 mmol$_{IL}$·g^{-1}, 0.1 mmol$_{Ru}$·g^{-1} theoretical) by (a) HAADF-STEM, (b, c) HAADF-STEM-EDX elemental mapping images of (b) Ru Lα and (c) Br Kα, (d) normalized Ru K-edge X-ray absorption near edge structure (XANES) spectra of Ru@SILP$_{AC}$ and reference materials, and (e) k^2-weighted R-space Fourier transformed extended X-ray absorption fine structure (FT-EXAFS) spectra of Ru@SILP$_{AC}$ and reference materials (without phase correction) and Ru foil with χ(0.5).

materials.[41] The metal loading was achieved by wet impregnation of the supports with a solution of [Ru(2-methylallyl)$_2$(cod)] (cod = 1,5-cyclooctadiene) in tetrahydrofuran (THF). After evaporation of the solvent under vacuum, the impregnated supports were subjected to an atmosphere of H_2 (50 bar) at 100 °C for 18 h, giving black powders with a theoretical Ru loading of 1 wt % (or 0.1 mmol·g^{-1}) (Figure 2). Ruthenium NPs were deposited on nonmodified activated carbon following the same protocol to provide the reference material Ru@AC. Characterization of Ru@SILP$_{AC}$ materials by N_2 physisorption showed lower Brunauer−Emmett−Teller (BET) surface areas (964−1725 $m^2 \cdot g^{-1}$) than for AC (2840 $m^2 \cdot g^{-1}$), as expected upon loading of IL and Ru NPs on the support (Table 1). Elemental analysis by inductively coupled plasma-optical emission spectrometry (ICP-OES) determined Ru loadings in the 0.07−0.09 mmol·g^{-1} range on all Ru@SILP$_{AC}$ samples, consistent with the theoretical Ru loading of 0.1 mmol·g^{-1} (Table 1).

High-angle annular dark field scanning transmission electron microscopy (HAADF-STEM) showed small (1.3−1.7 nm) and well-dispersed NPs on all supports (Table 1, Figures S4 and S5). Additionally, HAADF-STEM with energy dispersive X-ray spectroscopy (EDX) images of a selected Ru@SILP$_{AC}$ material evidenced the uniform distribution of IL and Ru NPs on the AC support (Figure 3a−c). The percentage of Ru atoms exposed on the NP surfaces was derived from the NP size by standard calculations as a basis for turnover frequency (TOF) determination (see Supporting Information Section 4.6.1 and Table S7 for details).

The Ru NPs in Ru@SILP$_{AC}$ and Ru@AC were characterized by using X-ray Absorption Spectroscopy (XAS) to investigate their electronic structure and coordination environment. The X-ray Absorption Near Edge Structure (XANES) spectra (Figure 3d) of Ru@SILP$_{AC}$ and Ru@AC reveal that both catalysts contain a mixture of metallic and oxidized Ru species. This is evidenced by their absorption edge positions, defined here as the energy position of the rising edge feature at half of the edge jump, which are 22,124.9 and 22,125.3 eV, respectively. These values are shifted to higher energies relative to Ru foil (22,119.5 eV) but remain below that of RuO_2 (22,127.3 eV). The nonphase shift corrected Fourier transformed Extended X-ray Absorption Fine Structure (EXAFS) spectra (Figure 3e) of both catalysts show features corresponding to Ru−O scattering at ∼1.5 Å and Ru−Ru scattering at ∼2.4 Å. However, the amplitudes of these features are significantly lower than those observed in RuO_2 and

https://doi.org/10.1021/acscatal.5c03605
ACS Catal. 2025, 15, 14601−14610

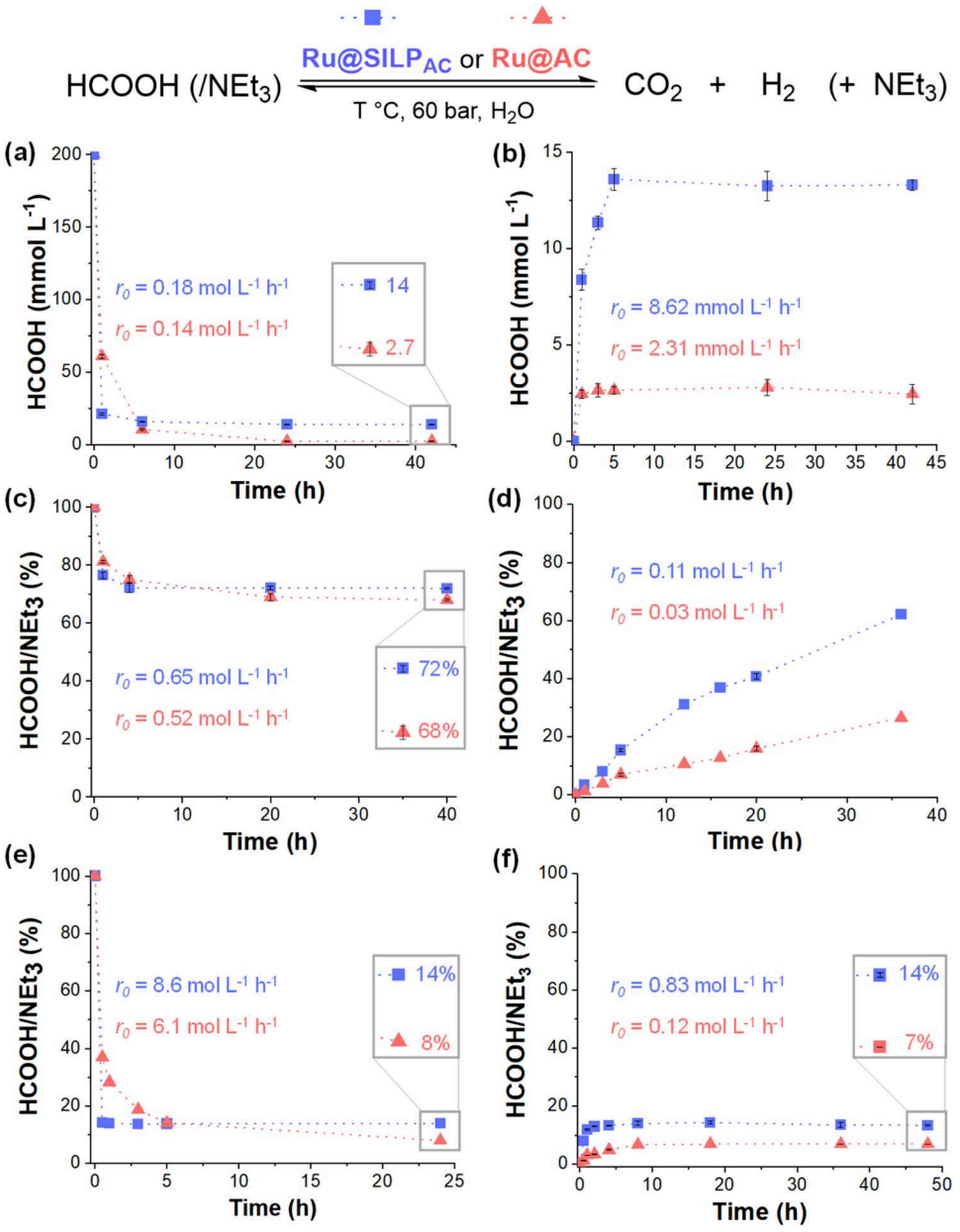

Figure 4. (a–f) Time profiles using Ru@SILP$_{AC}$ and Ru@AC (0.1 mmol·g^{-1} theoretical Ru loading) for (a) formic acid decomposition at 100 °C in H_2O, (b) formic acid synthesis at 100 °C in H_2O, (c) formic acid decomposition at 100 °C in aqueous NEt_3 solution, (d) formic acid formation at 100 °C in aqueous NEt_3 solution, (e) formic acid decomposition at 150 °C in aqueous NEt_3 solution, and (f) formic acid formation at 150 °C in aqueous NEt_3 solution. Reaction conditions are provided in the SI (Table S9). Data points are average values of 2–3 experiments, and error bars represent standard deviations.

metallic Ru, aligning with the partially oxidized nature of the Ru NPs, as inferred from the XANES analysis.

The EXAFS fitting results (Figure S6 and Table S8) indicate that the first-shell Ru–O coordination in both catalysts likely arises from two distinct Ru–O scattering paths at ∼1.85 and ∼2.01 Å. These paths result in a combined total coordination number (CN) of approximately 4.6 for Ru@SILP$_{AC}$ and 6.1 for Ru@AC. Given that EXAFS is not sufficiently sensitive to distinguish between light scatterers such as C and O at similar distances, and that typical Ru–O bond lengths (e.g., in RuO_2) exceed 1.94 Å, it is plausible that the shorter path at ∼1.85 Å corresponds to Ru–C bonds.[41] These bonds may originate from residual ligands from the Ru precursors or strong chemical interactions between the Ru NPs and the carbon support. Regarding the Ru–Ru coordination, the fitted results suggest Ru–Ru distances of 2.68 Å, consistent with those in hexagonal close-packed (hcp) metallic Ru. Although the Ru–Ru coordination numbers are relatively similar for Ru@SILP$_{AC}$ (3.0) and Ru@AC (2.7), the Debye–Waller (DW) factors differ significantly. The higher DW factor for Ru–Ru scattering in Ru@AC (0.0083) compared to that in Ru@SILP$_{AC}$ (0.0048) indicates that the Ru species in Ru@AC exhibit a more disordered coordination structure, despite both catalysts having similar particle size distributions. In summary, the Ru NPs in both Ru@SILP$_{AC}$ and Ru@AC are partially oxidized and poorly crystallized. However, the Ru species in Ru@SILP$_{AC}$ are relatively less oxidized and less disordered compared with those in Ru@AC.

https://doi.org/10.1021/acscatal.5c03605
ACS Catal. 2025, 15, 14601–14610

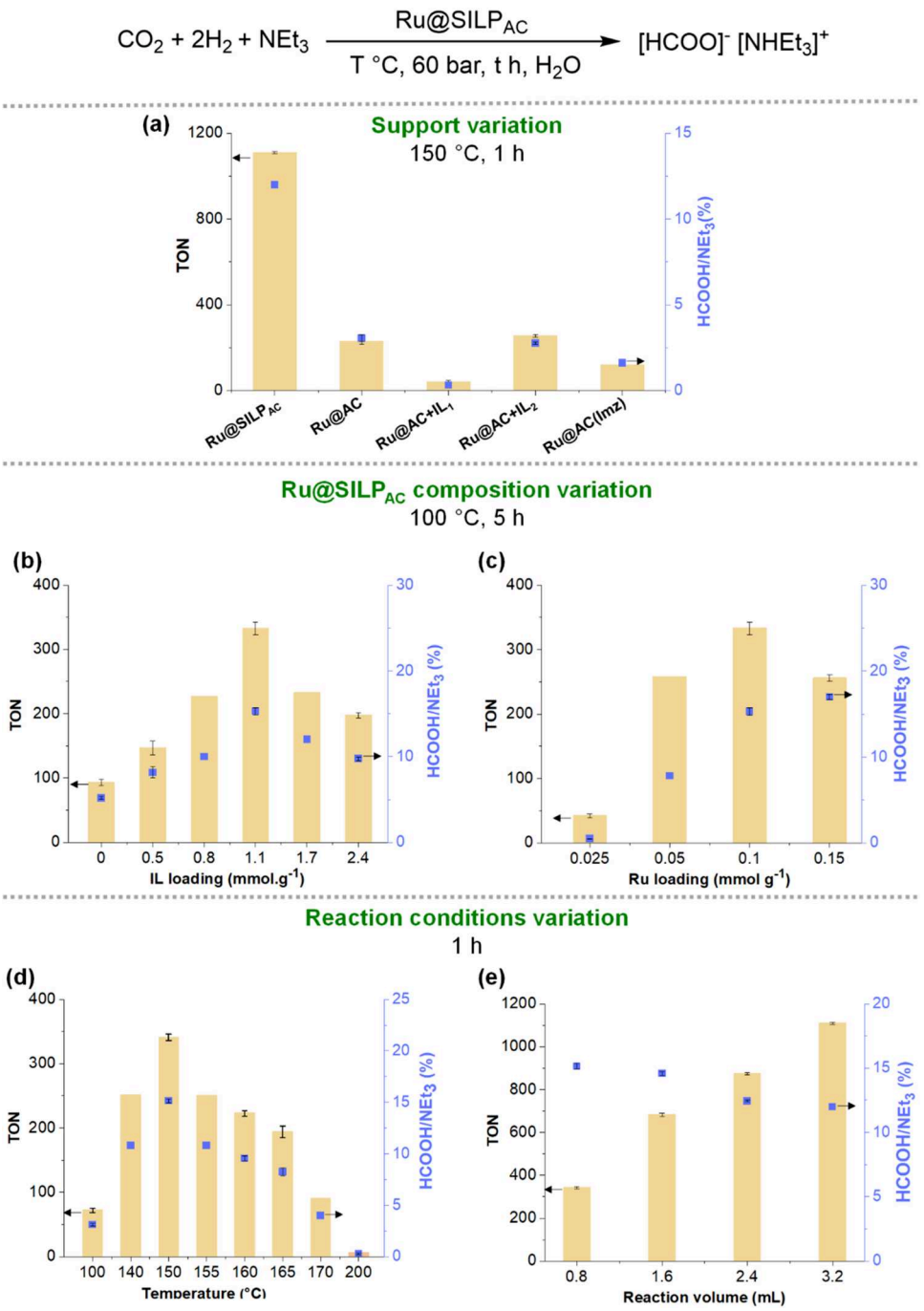

Figure 5. Hydrogenation of CO_2 in aqueous amine solution with (a) different catalysts (see Figure S9 for illustrations of catalysts structures), (b) Ru@SILP$_{AC}$ catalysts with varied IL loadings (fixed theoretical Ru loading of 0.1 $mmol_{Ru}·g^{-1}$), (c) Ru@SILP$_{AC}$ catalysts with varied Ru loadings (fixed IL loading of 1.1 $mmol_{IL}·g^{-1}$), (d) Ru@SILP$_{AC}$ at different temperatures, and (e) Ru@SILP$_{AC}$ in varied reaction volumes at constant H_2O/NEt_3 ratio. Detailed reaction conditions are provided in the SI (Tables S11−S14). TON has been estimated based on experimental Ru loadings and estimated surface Ru atoms. Data points are average values of 2−3 experiments, and error bars represent standard deviations.

Catalytic Study. The hydrogenation of CO_2 using Ru@ support catalysts was conducted in 15 mL stainless steel high-pressure reactors (unless otherwise specified in SI) equipped with a pressure gauge and heated in temperature-controlled aluminum blocks. The reactors were equipped with glass inlets charged with the catalyst material and solvent system under air and then pressurized sequentially with CO_2 and H_2. Once the heating blocks reached the target temperatures, the reaction mixtures were vigorously stirred with magnetic stir bars for the specified durations. Upon completion of the reaction, the gas phase was analyzed by gas chromatography (GC) using a flame ionization detector (FID) and a thermal conductivity detector (TCD).

The liquid phase was analyzed by ^{1}H NMR using 1,4-dioxane as internal standard to determine the amount of formic acid generated and the HCOOH/NEt_3 ratio (see Supporting Information for details). ^{1}H NMR analysis revealed deprotonation of the acid by NEt_3 to give triethylammonium formate in the aqueous system, as expected.[22] Other liquid or gaseous products were not detected (Figures S7 and S8).

https://doi.org/10.1021/acscatal.5c03605
ACS Catal. 2025, 15, 14601−14610

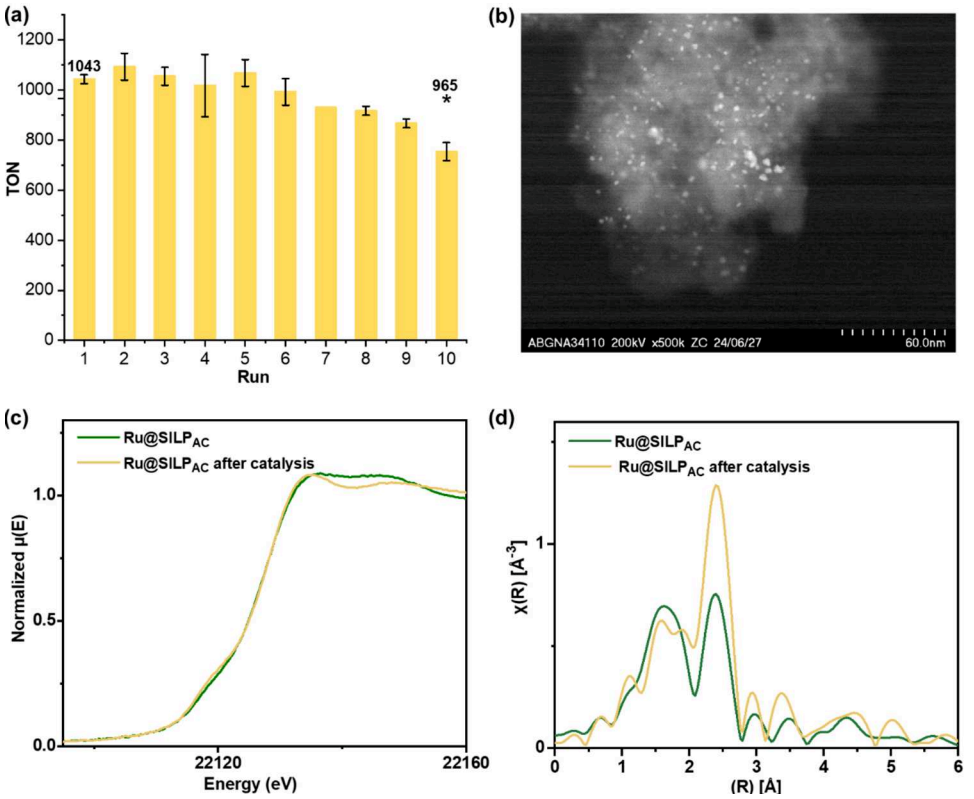

Figure 6. Stability and recyclability studies of Ru@SILP$_{AC}$ for hydrogenation of CO_2. (a) Recycling experiments, (b) HAADF-STEM image of Ru@SILP$_{AC}$ after Run-10, (c) normalized Ru K-edge XANES spectra of Ru@SILP$_{AC}$ before and after Run-1, and (d) k^2-weighted R-space FT-EXAFS spectra of Ru@SILP$_{AC}$ before and after Run-1 (without phase correction). Reaction conditions: Ru@SILP$_{AC}$ (50 mg, 1.1 mmol$_{IL}$·g^{-1}, 0.1 mmol$_{Ru}$·g^{-1} theoretical), 150 °C, 60 bar total pressure with CO_2/H_2 = 1:2, solvent system: NEt_3 (2.32 mL, 16.7 mmol) + H_2O (0.88 mL, 48.8 mmol), 1 h. TON has been estimated based on experimental Ru loadings and estimated surface Ru atoms. Data points are average values of 2−3 experiments, and error bars represent standard deviations.

Turnover numbers (TONs) and turnover frequencies (TOFs) were determined from the concentration of formate in solution and calculated based on the experimental Ru loading and the amount of Ru exposed at the surface of the NPs, estimated from the size of NPs (Table S7, SI).

The influence of the IL modification on the stabilization of formic acid and reaction equilibrium was investigated by comparing the performances of Ru@SILP$_{AC}$ and Ru@AC catalysts in CO_2 hydrogenation and formic acid decomposition reactions under a set of identical conditions (fixed total pressure of 60 bar with CO_2/H_2 = 1:2; 100 or 150 °C, in H_2O or aqueous NEt_3 solutions) (Figure 4). The first comparison was conducted in pure water as reaction medium. An excess of formic acid was charged in the reaction mixture and subjected to decomposition in order to determine the equilibrium concentration under the reaction conditions (Figure 4a). Formic acid rapidly decomposed at 100 °C in water in the presence of both catalysts, with Ru@SILP$_{AC}$ inducing a ca. 25% higher initial rate than Ru@AC (r_0 = 0.18 vs 0.14 mol·L^{-1}·h^{-1}). Even more significantly, the equilibrium concentration was more than 5 times higher with the IL-modified catalyst than with the unmodified material (14 vs 2.7 mmol·L^{-1}). The HCOOH concentrations achieved from catalytic CO_2 hydrogenation after 24 h matched well with the distinct equilibria determined (Figure 4b). Notably, the hydrogenation of CO_2 with Ru@SILP$_{AC}$ resulted in a nearly 4 times higher HCOOH production rate (r_0 = 8.6 mmol·L^{-1}·h^{-1}) than when Ru@AC was used (r_0 = 2.3 mmol·L^{-1}·h^{-1}).

Both Ru@SILP$_{AC}$ and Ru@AC catalyzed the decomposition of a 1:1 composition of the ammonium formate HCOOH/NEt_3 in H_2O at 100 °C, but again Ru@SILP$_{AC}$ provided a higher rate (r_0 = 0.62 mol·L^{-1}·h^{-1}) and equilibrium position (HCOOH/NEt_3 ratio of 72%) (Figure 4c). For the hydrogenation of CO_2 with Ru@SILP$_{AC}$, the recorded time profile shows an apparent zero-order increase (r_0 = 0.1 mol·L^{-1}·h^{-1}) in the HCOOH/NEt_3 ratio over time, reaching 62% after 36 h (TON = 1371), which is close to the equilibrium position of 72% (Figure 4d). In contrast, Ru@AC proved much slower (r_0 = 0.03 mol·L^{-1}·h^{-1}) and the equilibrium was far from being reached after 36 h (HCOOH/NEt_3 ratio of 27%). No induction period was observed under any of the tested conditions, indicating that catalytically active species are present from the start of the reaction (Figure 4, Table S10). The same trend was observed under hydrothermal conditions (150 °C), with the equilibrium position found, as expected, at much lower HCOOH/NEt_3 ratios and reached at much higher rates (Figure 4e,f).

These findings reveal that the IL-like modifier not only enhances the activity of Ru NPs in Ru@SILP$_{AC}$ but also substantially stabilizes the produced formic acid under various reaction conditions, leading to more favorable thermodynamic equilibria. Further investigations of the influence of metal−IL interactions focus on the hydrogenation of CO_2 in aqueous NEt_3 solutions.

The catalytic performance of Ru@SILP$_{AC}$ under standard conditions at 150 °C (TON = 1110, HCOOH/Et_3N ratio of

https://doi.org/10.1021/acscatal.5c03605
ACS Catal. 2025, 15, 14601−14610

12%, i.e., close to equilibrium) was found not only superior to that of Ru@AC (TON = 231, HCOOH/Et_3N ratio of 3%, i.e., far from equilibrium), but also of Ru NPs immobilized on other types of molecularly modified surfaces (MMS) supports (Figure 5a, and catalysts illustrated in Figure S9). In particular, physisorption of IL ([3-(4-aminophenethyl)-1-butyl-1*H*-imidazol-3-ium]bromide) on Ru@AC gave a catalytic system noted Ru@AC + IL_1 possessing very low activity (TON = 42), presumably due to strong interactions between the aniline functionality of IL and Ru NPs. Modifying the structure of the physisorbed IL to ([1-butyl-3-methyl-1*H*-imidazol-3-ium]-bromide) to prevent this presumed NPs poisoning by aniline functionalities led to a Ru@AC + IL_2 catalyst with performances similar to those of Ru@AC, without providing any substantial kinetic or thermodynamic benefit. Finally, Ru NPs immobilized on AC covalently modified by the non-IL [4-(2-(1*H*-imidazol-1-yl)ethyl)aniline] molecule in place of the imidazolium-based IL were found to be poorly active (TON = 121). These results demonstrate the requirement for intimate contact between the IL and Ru NPs components to observe synergistic effects.

Interestingly, the use of Ru@$SILP_{AC}$ catalysts with systematically varied IL and Ru loadings at 100 °C revealed a maximum formic acid production (TON = 333, HCOOH/NEt_3 ratio of 15%, far away from the thermodynamic limit of 72% at 100 °C) in the presence of intermediate IL and Ru loadings, i.e., 1.1 $mmol_{IL}·g^{-1}$ and 0.1 $mmol_{Ru}·g^{-1}$, respectively (Figure 5b,c, Tables S11 and S12). This may reflect the substantial impact of the ionic liquid layer on mass transport properties around the Ru active sites. The influence of the reaction temperature was tested using a reaction time of 1 h (Figure 5d, Table S13). Raising the temperature from 100 to 150 °C resulted in a faster reaction and an increase in the TON from 72 to 333, thereby reaching the previously determined maximum HCOOH/NEt_3 ratio of ca. 14% (Figure 4e). Above 150 °C, TONs and HCOOH/NEt_3 ratios dropped rapidly, with a trend presumably reflecting the position of the respective thermodynamic equilibria. Increasing the reaction volume (i.e., the amount of H_2O and NEt_3) at constant Ru@$SILP_{AC}$ loading allowed reaching a TON of 1110 while maintaining a HCOOH/NEt_3 ratio close to the thermodynamic limit (Figure 5e, Table S14).

Scaling up the reaction from a volume of 3.2−80 mL under optimized reaction conditions while keeping the amount of catalyst and NEt_3/H_2O molar ratio constant allowed reaching an estimated TOF of 3126 h^{-1}, which is among the highest ever reported for NPs-based catalysts. After 20 h, a TON of 14,780 with a HCOOH/NEt_3 ratio of 6% was obtained.

The reusability and robustness of the Ru@$SILP_{AC}$ catalyst were investigated through recycling experiments conducted for cycles of 1 h under the following harsh hydrothermal conditions: total pressure of 60 bar with CO_2/H_2 = 1:2; 150 °C, total volume: 3.2 mL; NEt_3/H_2O (v/v) = 2.6. It is worth noting that these conditions were selected specifically to investigate and highlight catalyst stability and are not particularly relevant for practical application due to the low equilibrium limit. Satisfyingly, the Ru@$SILP_{AC}$ catalyst maintained its activity for at least 10 cycles (Figure 6a and Table S15). The slight decrease in TON over the cycles is attributed to minor material losses during catalyst separation by centrifugation and washing, consistent with the reduced mass of catalyst (39 mg instead of 50 mg) recovered after 10 cycles. Accounting for this mass loss in the calculation gave a TON value of 965 at cycle 10, very close to the TON provided by the fresh catalyst (1043 at cycle 1).

Characterization by TGA (Figure S10a) and N_2 adsorption (Table S15) of Ru@$SILP_{AC}$ after 10 cycles showed no decrease in weight loss or BET surface area compared to the pristine catalyst, indicating the absence of substantial IL leaching. The loss of Br, as evidenced by XPS analysis (Figure S10b), is presumably due to the replacement of the bromine anions by formate anions under reaction conditions without a noticeable impact on the catalytic properties. Variations of the Ru loading on Ru@$SILP_{AC}$ characterized by ICP-OES were found within the measurement error (Table S15). HAADF-STEM of the catalyst after 10 cycles revealed well-dispersed Ru NPs with slightly larger sizes (1.6 ± 0.3 nm, Figures 6b and S11).

Interestingly, the size distribution of the same NPs was determined after 1 cycle (Figure S12), indicating that Ru NPs undergo a rapid growth to ca. 1.6 nm upon exposure to the reaction conditions and then maintain their size throughout the following nine cycles. Ru K-edge XANES analysis of Ru@$SILP_{AC}$ before and after catalysis showed overlapping edge positions, thus no noticeable change in the electronic properties of Ru NPs (Figure 6c). The EXAFS fitting results revealed a slightly higher Ru−Ru CN (5.0 ± 0.5) in comparison to Ru@$SILP_{AC}$ before catalysis (Ru−Ru CN of 3.0 ± 0.6), which could be possibly due to larger and more reduced NPs; all the fitting results are summarized in Table S8, SI (Figure 6d). These data demonstrate the stability of the Ru@$SILP_{AC}$ catalyst, which outperforms by far that of previously reported catalysts (including SiO_2-based Ru@SILP[41]) used under even milder conditions (Table S16).

The recyclability of Ru@$SILP_{AC}$ and Ru@AC was also compared at 100 °C. Notably, the catalytic performance of Ru@AC declined rapidly under these conditions (by more than 60% in 5 cycles), while Ru@$SILP_{AC}$ remained stable (Figure S13). Thus, Ru@$SILP_{AC}$ is not only substantially more active than Ru@AC, but also much more stable, further substantiating the benefits of using an SILP-type support material for Ru NPs. An illustration of the hydrogenation of CO_2 at the surface of Ru@$SILP_{AC}$ including the key role(s) of the different catalyst components is provided in Figure S14.

Interestingly, the Ru@$SILP_{AC}$ catalyst could reversibly hydrogenate CO_2 to formic acid and dehydrogenate the formic acid back to CO_2 and H_2, as demonstrated through 4 cycles (Figure S15).

CONCLUSIONS

In summary, we report the development of a new generation of water-stable SILP materials using activated carbon as a support and diazotization as a robust grafting strategy for imidazolium-based ionic liquids. Corresponding Ru@$SILP_{AC}$ catalysts were prepared and fully characterized by a combination of techniques including ICP-OES, TGA, N_2 physisorption, FT-IR, electron microscopy, XPS, and XAS. Ru@$SILP_{AC}$ was found to possess superior performance as compared to Ru@AC and other reference catalysts, which we attribute to the favorable environment provided by the IL layer to the Ru NPs, potentially resulting in beneficial electronic interactions and improved mass transport. Most importantly, the presence of the IL provided not only higher catalytic activity for Ru NPs, but also enhanced stabilization for formic acid, thereby shifting the equilibrium of the reaction. The stability and recyclability of Ru@$SILP_{AC}$ in water/amine media at 100 and 150 °C were

https://doi.org/10.1021/acscatal.5c03605
ACS Catal. 2025, 15, 14601−14610

found excellent over 10 reaction cycles, in contrast to the Ru@AC reference that rapidly deactivated.

In general terms, the synthetic methodology to prepare hydrothermally stable supports with molecularly modified surfaces presented here is very versatile. In combination with the organometallic approach for the deposition of NPs, it opens access to a wide range of multifunctional, water-stable catalyst materials. Therefore, this method can broaden the range of potential applications of such tailor-made catalysts for transformations occurring in aqueous solution or producing water as a byproduct, for example, in biomass conversion.

EXPERIMENTAL SECTION

Synthesis of $SILP_{AC}$. The $SILP_{AC}$ was synthesized using a previously reported diazotization method for small organic molecules.[41,48] Under an inert atmosphere, predried activated carbon (AC) and ionic liquid (IL) were dispersed in acetonitrile in a round-bottom flask. Isoamylnitrite was then added while keeping the flask in the dark. The reaction mixture was stirred at 60 °C and 700 rpm for 18 h under dark and inert conditions. After it was cooled, the reaction mixture was filtered, and the resulting solid was washed sequentially with acetonitrile and water. The final product, $SILP_{AC}$, was obtained as a black solid. The detailed method for calculating the IL loadings on the synthesized $SILP_{AC}$ is given in the SI.

Synthesis of Ru@Support. The Ru@support catalysts were prepared by immobilizing Ru nanoparticles (NPs) onto various support materials following a previously reported procedure from our group.[41] Under an inert atmosphere, a solution of [Ru(2-methylallyl)$_2$(cod)] in tetrahydrofuran (THF) was added to the support material. The mixture was stirred at room temperature for 1 h. Subsequently, the solvent was evaporated, and the resulting impregnated powder was subjected to a hydrogen pressure (50 bar) and heated at 100 °C for 18 h. This process yielded the final catalyst, Ru@support, which was characterized using techniques including ICP-OES, TGA, N_2 physisorption, FT-IR, electron microscopy, XPS, and XAS.

Catalytic Experiments. All catalytic experiments were conducted in a high-pressure autoclave, with safety procedures described in SI. In a typical experiment, Ru@support, triethylamine, and water were added to a glass inlet, which was then transferred to the autoclave under ambient air. The reaction was carried out under a gas mixture of CO_2 and H_2 (1:2 ratio, total pressure 60 bar) at the desired temperature, with stirring in an aluminum heating block. After completion, the autoclave was cooled to room temperature and carefully depressurized. The gas phase was analyzed by gas chromatography using TCD/FID detectors, and the liquid phase was analyzed by ^{1}H NMR spectroscopy with 1,4-dioxane as an internal standard. Turnover numbers were determined using the following equation:

$$\mathrm{TON} = \frac{n_{\mathrm{formate}}}{n\mathrm{Ru} \times \%\ \mathrm{surface\ Ru}}$$

Detailed information about the methods and quantities used for the synthesis of IL, $SILP_{AC}$, Ru@support, and catalytic hydrogenation reactions is all provided in the SI.

ASSOCIATED CONTENT

Data Availability Statement

The data that support the findings of this study are available in the Supporting Information of this article. In addition, the data utilized in this study will be available for download on Edmond, the open data repository of the Max Planck Society, at https://doi.org/10.17617/3.LW2FXL.

Supporting Information

The Supporting Information is available free of charge at https://pubs.acs.org/doi/10.1021/acscatal.5c03605.

Synthesis of ionic liquid; synthesis and characterization of Ru@SILPs; detailed procedures for catalytic reactions; details for thermodynamic and kinetic studies; NMR and GC analyses; and X-ray absorption spectroscopic analysis (PDF)

AUTHOR INFORMATION

Corresponding Authors

Walter Leitner − *Max Planck Institute for Chemical Energy Conversion, 45470 Mülheim an der Ruhr, Germany; Institut für Technische und Makromolekulare Chemie, RWTH Aachen University, 52074 Aachen, Germany;* orcid.org/0000-0001-6100-9656; Email: walter.leitner@cec.mpg.de

Alexis Bordet − *Max Planck Institute for Chemical Energy Conversion, 45470 Mülheim an der Ruhr, Germany;* orcid.org/0000-0003-0133-3416; Email: alexis.bordet@cec.mpg.de

Authors

Neha Antil − *Max Planck Institute for Chemical Energy Conversion, 45470 Mülheim an der Ruhr, Germany*

Savarithai Jenani Louis Anandaraj − *Max Planck Institute for Chemical Energy Conversion, 45470 Mülheim an der Ruhr, Germany; Institut für Technische und Makromolekulare Chemie, RWTH Aachen University, 52074 Aachen, Germany*

Liqun Kang − *Max Planck Institute for Chemical Energy Conversion, 45470 Mülheim an der Ruhr, Germany;* orcid.org/0000-0003-2100-4310

Hooman Ghazi Zahedi − *Max Planck Institute for Chemical Energy Conversion, 45470 Mülheim an der Ruhr, Germany; Institut für Technische und Makromolekulare Chemie, RWTH Aachen University, 52074 Aachen, Germany*

Serena DeBeer − *Max Planck Institute for Chemical Energy Conversion, 45470 Mülheim an der Ruhr, Germany;* orcid.org/0000-0002-5196-3400

Complete contact information is available at: https://pubs.acs.org/10.1021/acscatal.5c03605

Funding

Open access funded by Max Planck Society.

Notes

The authors declare no competing financial interest.

ACKNOWLEDGMENTS

The authors acknowledge financial support by the Max Planck Society and by the Deutsche Forschungsgemeinschaft (DFG, German Research Foundation) under Germany's Excellence Strategy—Exzellenzcluster 2186 "The Fuel Science Center" ID: 390919832. The authors thank Daniela Sorokin for help with experimental work. The authors thank Jacob Johny for XPS measurements. The authors would like to thank Norbert Pfänder (Max Planck Institute for Chemical Energy Conversion) and Alin Benice Schöne (Max-Planck-Institut für Kohlenforschung) for TEM and STEM/EDX analysis. The authors would like to thank Marius Heise-Podleska and

Johanna Taing (Max Planck Institute for Chemical Energy Conversion) for measuring thermogravimetric Analysis and N_2 physisorption measurements. The authors are also thankful to Annika Gurowski, Alina Jakubowski, and Justus Werkmeister (Max Planck Institute for Chemical Energy Conversion) for GC and XRF measurements. The authors also acknowledge DESY (Hamburg, Germany), a member of the Helmholtz Association HGF, for the provision of experimental facilities. Parts of this research were carried out at PETRA III and the authors would like to thank Dr. Edmund Welter for assistance in using P65 beamline for XAS measurements (proposal No. I-20230324). L.K. acknowledges the Alexander von Humboldt Foundation for postdoctoral fellowship and funding support.

REFERENCES

(1) Aresta, M.; Dibenedetto, A.; Angelini, A. Catalysis for the Valorization of Exhaust Carbon: from CO_2 to Chemicals, Materials, and Fuels. Technological Use of CO_2. *Chem. Rev.* **2014**, *114*, 1709−1742.

(2) Artz, J.; Müller, T. E.; Thenert, K.; Kleinekorte, J.; Meys, R.; Sternberg, A.; Bardow, A.; Leitner, W. Sustainable Conversion of Carbon Dioxide: An Integrated Review of Catalysis and Life Cycle Assessment. *Chem. Rev.* **2018**, *118*, 434−504.

(3) Galán-Martín, Á.; Tulus, V.; Díaz, I.; Pozo, C.; Pérez-Ramírez, J.; Guillén-Gosálbez, G. Sustainability footprints of a renewable carbon transition for the petrochemical sector within planetary boundaries. *One Earth* **2021**, *4*, 565−583.

(4) Araújo, T. P.; Mitchell, S.; Pérez-Ramírez, J. Design Principles of Catalytic Materials for CO_2 Hydrogenation to Methanol. *Adv. Mater.* **2024**, *36*, No. 2409322.

(5) LeClerc, H. O.; Erythropel, H. C.; Backhaus, A.; Lee, D. S.; Judd, D. R.; Paulsen, M. M.; Ishii, M.; Long, A.; Ratjen, L.; Gonsalves Bertho, G.; et al. The CO_2 Tree: The Potential for Carbon Dioxide Utilization Pathways. *ACS Sustainable Chem. Eng.* **2025**, *13*, 5−29.

(6) Olah, G. A.; Goeppert, A.; Prakash, G. K. S. Chemical Recycling of Carbon Dioxide to Methanol and Dimethyl Ether: From Greenhouse Gas to Renewable, Environmentally Carbon Neutral Fuels and Synthetic Hydrocarbons. *J. Org. Chem.* **2009**, *74*, 487−498.

(7) Boddien, A.; Gärtner, F.; Federsel, C.; Sponholz, P.; Mellmann, D.; Jackstell, R.; Junge, H.; Beller, M. CO_2-"Neutral" Hydrogen Storage Based on Bicarbonates and Formates. *Angew. Chem., Int. Ed.* **2011**, *50*, 6411−6414.

(8) Centi, G.; Quadrelli, E. A.; Perathoner, S. Catalysis for CO_2 conversion: a key technology for rapid introduction of renewable energy in the value chain of chemical industries. *Energy Environ. Sci.* **2013**, *6*, 1711−1731.

(9) Álvarez, A.; Bansode, A.; Urakawa, A.; Bavykina, A. V.; Wezendonk, T. A.; Makkee, M.; Gascon, J.; Kapteijn, F. Challenges in the Greener Production of Formates/Formic Acid, Methanol, and DME by Heterogeneously Catalyzed CO_2 Hydrogenation Processes. *Chem. Rev.* **2017**, *117*, 9804−9838.

(10) Bai, S.-T.; De Smet, G.; Liao, Y.; Sun, R.; Zhou, C.; Beller, M.; Maes, B. U. W.; Sels, B. F. Homogeneous and heterogeneous catalysts for hydrogenation of CO_2 to methanol under mild conditions. *Chem. Soc. Rev.* **2021**, *50*, 4259−4298.

(11) Shang, X.; Liu, G.; Su, X.; Huang, Y.; Zhang, T. A review of the recent progress on direct heterogeneous catalytic CO_2 hydrogenation to gasoline-range hydrocarbons. *EES Catal.* **2023**, *1*, 353−368.

(12) Araújo, T. P.; Morales-Vidal, J.; Zou, T.; Agrachev, M.; Verstraeten, S.; Willi, P. O.; Grass, R. N.; Jeschke, G.; Mitchell, S.; López, N.; et al. Design of Flame-Made ZnZrO Catalysts for Sustainable Methanol Synthesis from CO_2. *Adv. Energy Mater.* **2023**, *13*, No. 2204122.

(13) Li, Y.; Zeng, L.; Pang, G.; Wei, X.; Wang, M.; Cheng, K.; Kang, J.; Serra, J. M.; Zhang, Q.; Wang, Y. Direct conversion of carbon dioxide into liquid fuels and chemicals by coupling green hydrogen at high temperature. *Appl. Catal., B* **2023**, *324*, No. 122299.

(14) Leitner, W. Carbon Dioxide as a Raw Material: The Synthesis of Formic Acid and Its Derivatives from CO_2. *Angew. Chem., Int. Ed.* **1995**, *34*, 2207−2221.

(15) Mellmann, D.; Sponholz, P.; Junge, H.; Beller, M. Formic acid as a hydrogen storage material − development of homogeneous catalysts for selective hydrogen release. *Chem. Soc. Rev.* **2016**, *45*, 3954−3988.

(16) Rumayor, M.; Dominguez-Ramos, A.; Irabien, A. Formic acid manufacture: carbon dioxide utilization alternatives. *Appl. Sci.* **2018**, *8*, 914.

(17) Yang, S.; An, H.; Arnouts, S.; Wang, H.; Yu, X.; de Ruiter, J.; Bals, S.; Altantzis, T.; Weckhuysen, B. M.; van der Stam, W. Halide-guided active site exposure in bismuth electrocatalysts for selective CO_2 conversion into formic acid. *Nat. Catal.* **2023**, *6*, 796−806.

(18) Sang, R.; Stein, C. A. M.; Schareina, T.; Hu, Y.; Léval, A.; Massa, J.; Turan, V.; Sponholz, P.; Wei, D.; Jackstell, R.; et al. Development of a practical formate/bicarbonate energy system. *Nat. Commun.* **2024**, *15*, No. 7268.

(19) Jessop, P. G.; Joó, F.; Tai, C.-C. Recent advances in the homogeneous hydrogenation of carbon dioxide. *Coord. Chem. Rev.* **2004**, *248*, 2425−2442.

(20) Moret, S.; Dyson, P. J.; Laurenczy, G. Direct synthesis of formic acid from carbon dioxide by hydrogenation in acidic media. *Nat. Commun.* **2014**, *5*, No. 4017.

(21) Sordakis, K.; Tang, C.; Vogt, L. K.; Junge, H.; Dyson, P. J.; Beller, M.; Laurenczy, G. Homogeneous Catalysis for Sustainable Hydrogen Storage in Formic Acid and Alcohols. *Chem. Rev.* **2018**, *118*, 372−433.

(22) Liu, Q.; Yang, X.; Li, L.; Miao, S.; Li, Y.; Li, Y.; Wang, X.; Huang, Y.; Zhang, T. Direct catalytic hydrogenation of CO_2 to formate over a Schiff-base-mediated gold nanocatalyst. *Nat. Commun.* **2017**, *8*, No. 1407.

(23) Sun, R.; Liao, Y.; Bai, S.-T.; Zheng, M.; Zhou, C.; Zhang, T.; Sels, B. F. Heterogeneous catalysts for CO_2 hydrogenation to formic acid/formate: from nanoscale to single atom. *Energy Environ. Sci.* **2021**, *14*, 1247−1285.

(24) Alli, Y. A.; Oladoye, P. O.; Ejeromedoghene, O.; Bankole, O. M.; Alimi, O. A.; Omotola, E. O.; Olanrewaju, C. A.; Philippot, K.; Adeleye, A. S.; Ogunlaja, A. S. Nanomaterials as catalysts for CO_2 transformation into value-added products: A review. *Sci. Total Environ.* **2023**, *868*, No. 161547.

(25) Upadhyay, P. R.; Srivastava, V. Ionic Liquid Mediated in Situ Synthesis of Ru Nanoparticles for CO_2 Hydrogenation Reaction. *Catal. Lett.* **2017**, *147*, 1051−1060.

(26) Qadir, M. I.; Weilhard, A.; Fernandes, J. A.; de Pedro, I.; Vieira, B. J. C.; Waerenborgh, J. C.; Dupont, J. Selective Carbon Dioxide Hydrogenation Driven by Ferromagnetic RuFe Nanoparticles in Ionic Liquids. *ACS Catal.* **2018**, *8*, 1621−1627.

(27) Qadir, M. I.; Bernardi, F.; Scholten, J. D.; Baptista, D. L.; Dupont, J. Synergistic CO_2 hydrogenation over bimetallic Ru/Ni nanoparticles in ionic liquids. *Appl. Catal., B* **2019**, *252*, 10−17.

(28) Sasaki, T. CO_2 hydrogenation in ionic liquids: Recent update. *Curr. Opin. Green Sustainable Chem.* **2022**, *36*, No. 100633.

(29) Webber, R.; Qadir, M. I.; Castegnaro, M. V.; Pontes, R. B.; da Silva, K. I. M.; Dupont, J. Unlocking dynamic intermetallic synergy: Ir/Ni alloy nanoparticles catalyze CO_2 hydrogenation to formic acid in ionic liquid environments. *J. Catal.* **2024**, *439*, No. 115791.

(30) Weilhard, A.; Qadir, M. I.; Sans, V.; Dupont, J. Selective CO_2 Hydrogenation to Formic Acid with Multifunctional Ionic Liquids. *ACS Catal.* **2018**, *8*, 1628−1634.

(31) Weilhard, A.; Argent, S. P.; Sans, V. Efficient carbon dioxide hydrogenation to formic acid with buffering ionic liquids. *Nat. Commun.* **2021**, *12*, No. 231.

(32) Piccirilli, L.; Rabell, B.; Padilla, R.; Riisager, A.; Das, S.; Nielsen, M. Versatile CO_2 Hydrogenation−Dehydrogenation Catalysis with a Ru−PNP/Ionic Liquid System. *J. Am. Chem. Soc.* **2023**, *145*, 5655−5663.

(33) Suhail, Z.; Koch, C. J.; Goeppert, A.; Prakash, G. S. Improved CO_2 conversion to methanol promoted by ionic liquid additives using

https://doi.org/10.1021/acscatal.5c03605
ACS Catal. 2025, 15, 14601−14610

a Cu/ZnO/Al_2O_3 heterogeneous catalyst. *Chem. Commun.* **2025**, *61*, 7688−7691.
(34) Haumann, M.; Wasserscheid, P. SILP and SCILL Catalysis. In *Catalysis in Ionic Liquids: From Catalyst Synthesis to Application*; Hardacre, C.; Parvulescu, V., Eds.; The Royal Society of Chemistry: United Kingdom, 2014; p 15.
(35) Bordet, A.; Leitner, W. Metal nanoparticles immobilized on molecularly modified surfaces: versatile catalytic systems for controlled hydrogenation and hydrogenolysis. *Acc. Chem. Res.* **2021**, *54*, 2144−2157.
(36) Bordet, A.; Moos, G.; Welsh, C.; Licence, P.; Luska, K. L.; Leitner, W. Molecular Control of the Catalytic Properties of Rhodium Nanoparticles in Supported Ionic Liquid Phase (SILP) Systems. *ACS Catal.* **2020**, *10*, 13904−13912.
(37) Rengshausen, S.; Van Stappen, C.; Levin, N.; Tricard, S.; Luska, K. L.; DeBeer, S.; Chaudret, B.; Bordet, A.; Leitner, W. Organometallic Synthesis of Bimetallic Cobalt-Rhodium Nanoparticles in Supported Ionic Liquid Phases (Co_xRh_{100-x}@SILP) as Catalysts for the Selective Hydrogenation of Multifunctional Aromatic Substrates. *Small* **2021**, *17*, No. 2006683.
(38) Levin, N.; Goclik, L.; Walschus, H.; Antil, N.; Bordet, A.; Leitner, W. Decarboxylation and Tandem Reduction/Decarboxylation Pathways to Substituted Phenols from Aromatic Carboxylic Acids Using Bimetallic Nanoparticles on Supported Ionic Liquid Phases as Multifunctional Catalysts. *J. Am. Chem. Soc.* **2023**, *145*, 22845−22854.
(39) Díaz, U.; Brunel, D.; Corma, A. Catalysis using multifunctional organosiliceous hybrid materials. *Chem. Soc. Rev.* **2013**, *42*, 4083−4097.
(40) van Deelen, T. W.; Hernández Mejía, C.; de Jong, K. P. Control of metal-support interactions in heterogeneous catalysts to enhance activity and selectivity. *Nat. Catal.* **2019**, *2*, 955−970.
(41) Louis Anandaraj, S. J.; Kang, L.; DeBeer, S.; Bordet, A.; Leitner, W. Catalytic Hydrogenation of CO_2 to Formate Using Ruthenium Nanoparticles Immobilized on Supported Ionic Liquid Phases. *Small* **2023**, *19*, No. 2206806.
(42) Lu, J.; Wang, L.; Sun, X.; Li, X.; Liu, X. Absorption of CO_2 into Aqueous Solutions of Methyldiethanolamine and Activated Methyldiethanolamine from a Gas Mixture in a Hollow Fiber Contactor. *Ind. Eng. Chem. Res.* **2005**, *44*, 9230−9238.
(43) Scott, M.; Blas Molinos, B.; Westhues, C.; Franciò, G.; Leitner, W. Aqueous Biphasic Systems for the Synthesis of Formates by Catalytic CO_2 Hydrogenation: Integrated Reaction and Catalyst Separation for CO_2-Scrubbing Solutions. *ChemSusChem* **2017**, *10*, 1085−1093.
(44) Kopitha, K.; Elakneswaran, Y.; Kitagaki, R.; Saito, R.; Tsujino, M.; Nishida, A.; Senboku, H.; Hiroyoshi, N. N-methyldiethanolamine (MDEA) as an effective CO_2 absorbent for direct air capture (DAC) in cement-based materials. *Chem. Eng. J.* **2023**, *475*, No. 146067.
(45) Elek, J.; Nádasdi, L.; Papp, G.; Laurenczy, G.; Joó, F. Homogeneous hydrogenation of carbon dioxide and bicarbonate in aqueous solution catalyzed by water-soluble ruthenium(II) phosphine complexes. *Appl. Catal., A* **2003**, *255*, 59−67.
(46) Connelly Robinson, S. J.; Zall, C. M.; Miller, D. L.; Linehan, J. C.; Appel, A. M. Solvent influence on the thermodynamics for hydride transfer from bis(diphosphine) complexes of nickel. *Dalton Trans.* **2016**, *45*, 10017−10023.
(47) Bello, T. O.; Bresciani, A. E.; Nascimento, C. A. O.; Alves, R. M. B. Thermodynamic analysis of carbon dioxide hydrogenation to formic acid and methanol. *Chem. Eng. Sci.* **2021**, *242*, No. 116731.
(48) Rajkumar, T.; Ranga Rao, G. Synthesis and characterization of hybrid molecular material prepared by ionic liquid and silicotungstic acid. *Mater. Chem. Phys.* **2008**, *112*, 853−857.
(49) Wang, B.; Lai, H.; Yue, Y.; Sheng, G.; Deng, Y.; He, H.; Guo, L.; Zhao, J.; Li, X. Zeolite Supported Ionic Liquid Catalysts for the Hydrochlorination of Acetylene. *Catalysts* **2018**, *8*, 351.
(50) Wan, X.; Xiang, X.; Tang, S.; Yu, D.; Huang, H.; Hu, Y. Immobilization of Candida antarctic lipase B on MWNTs modified by ionic liquids with different functional groups. *Colloids Surf., B* **2017**, *160*, 416−422.
(51) Gan, C.; Liang, T.; Li, W.; Fan, X.; Zhu, M. Amine-terminated ionic liquid modified graphene oxide/copper nanocomposite toward efficient lubrication. *Appl. Surf. Sci.* **2019**, *491*, 105−115.

https://doi.org/10.1021/acscatal.5c03605
ACS Catal. 2025, 15, 14601−14610

Ruthenium Nanoparticles on Water-Stable Supported Ionic Liquid Phases as Catalytic Systems for Aqueous Phase CO_2 Hydrogenation

Neha Antil,[a] Savarithai Jenani Louis Anandaraj,[a,b] Liqun Kang,[a] Hooman Ghazi Zahedi,[a,b] Serena DeBeer,[a] Walter Leitner,[a,b] Alexis Bordet[a]**

[a]Max Planck Institute for Chemical Energy Conversion, Stiftstraße 34-36, 45470 Mülheim an der Ruhr, Germany.

[b]Institut für Technische und Makromolekulare Chemie, RWTH Aachen University, Worringerweg 2, 52074 Aachen, Germany

*Corresponding authors: walter.leitner@cec.mpg.de / alexis.bordet@cec.mpg.de

Contents

1. Safety Warning

High-pressure experiments with compressed gases must be carried out only with appropriate equipment and under rigorous safety precautions. In this study, high-pressure autoclaves capable of withstanding up to 200 bar are utilized, with 60 bar as the maximum pressure applied at room temperature. After the hydrogenation reaction, hydrogen is safely vented from the reactor in a fume hood. Scaled-up reactions were performed in a 115 mL stainless steel high-pressure batch reactor equipped with a pressure gauge and mechanical stirrer, and heated with a temperature-controlled clamp-on band heater. Before working with 1,4-dioxane, ensure proper training on its handling and storage. Store 1,4-dioxane in a cool, dry, and well-ventilated location, away from light and oxidizing agents to prevent the formation of dangerous peroxides. Avoid ignition sources, including smoking and open flames, in areas where 1,4-dioxane is used or stored.

2. General

2.1. Chemicals and Synthesis

The synthesis of ionic liquids (ILs), Supported Ionic Liquid Phases (SILP), and Ru@$SILP_{AC}$ was carried out under an inert atmosphere using standard Schlenk techniques or in a glovebox unless stated otherwise. All synthesized ILs, $SILP_{AC,}$ and Ru@$SILP_{AC}$ were stored under air. All the catalysis reaction mixtures have been prepared under air before pressurizing them with CO_2 and H_2. All the NMR samples were prepared in air, and 1,4-dioxane was used as an internal standard (IS). All chemicals and solvents were purchased from commercial sources and used without purification, as listed below.

Chemicals	Abbreviation	Purity	Origin
4-Nitrophenylethyl bromide		>98.0%	TCI Deutschland GmbH
1-Butyl imidazole		>98%	Sigma Aldrich
Toluene		>99.8%	Carl Roth GmbH + Co. KG
Heptane		>99.8%	Carl Roth GmbH + Co. KG
Dichlormethane	DCM	>99.5	Carl Roth GmbH + Co. KG

Imidazole		≥99%	Sigma-Aldrich
Sodium hydride	NaH	≥99%	Sigma-Aldrich
Activated Carbon	AC		Nuchar, (batch no. SA 1500 3-R-19)
Isopentyl nitrite		96%	Alfa Aesar
1-Butyl-3-methylimidazolium Bromide		>98%	TCI Deutschland GmbH
Bis(2-methylallyl)(1,5-cyclooctadiene)ruthenium(II)	[Ru(2-methylallyl)$_2$(cod)]	97%	ABCR GmbH
Tetrahydrofuran	THF	>99.5%	Carl Roth GmbH + Co. KG
Triethylamine	NEt_3	99%	Sigma Aldrich
1,4-Dioxane		≥99,8 % (≤100 ppm H_2O), stabilized	Carl Roth GmbH + Co. KG
Formic acid	HCOOH	≥95%	Sigma-Aldrich

3. Analytics

- Liquid state NMR spectra were recorded on a Bruker AV-400 spectrometer. The coupling constants (*J*) are given in Hertz (Hz), and the chemical shifts (δ) are expressed in ppm relative to TMS at 298 K. The peak patterns are indicated as follows: *s* = singlet; *d* = doublet; *t* = triplet, *q* = quartet, *m* = multiplet.

- N_2 physisorption measurements were performed on a Quadrasorb SI (Quantachrom Instruments). Before the measurements, the samples were degassed under vacuum at 200 °C for 8 h. The specific surface area was evaluated using the BET method and adsorption data in the range of relative pressure p/p_0 = 0.05 - 0.25. All the measurements were performed by Johanna Taing.

- Thermogravimetric analysis (TGA) was performed on a PerkinElmer TGA 8000 coupled with Clarus 600T MS. The samples were heated to 1000 °C with a heating rate of 50 °C/min in an Ar atmosphere. All the measurements were performed by Marius Heise-Podleska and Johanna Taing.

- Electrospray ionization mass spectrometry (ESI-MS) was carried out using ESQ 3000 (Bruker), Thermo Scientific LTQ-FT or Thermo Scientific Exactive.

- High-resolution mass spectrometry (HRMS) was measured using Bruker APEX III FT-MS (7 T magnet), MAT 95 (Finnigan), Thermo Scientific LTQ-FT, or Thermo Scientific Exactive.

- FT-IR measurements were carried out in ATR mode under an air atmosphere.

- Shimadzu GC-2030 equipped with a Thermal conductivity detector (TCD) and Flame Ionization detector (FID) was used for all the Gas Chromatography (GC) measurements.

- Inductively Coupled Plasma Optical Emission Spectroscopy (ICP-OES) was carried out by Mikroanalytisches Labor Kolbe on an ICP-OES Spectro Arcos from Spectro. The sample preparation was performed using a CEM-Mars 6 microwave.

- X-ray Fluorescence (XRF) was performed using a spectro Xepos C with a prolene foil of 12 µm at 3keV to 19 keV.

- High-angle annular dark-field scanning transmission electron microscopy (HAADF-STEM) was performed on a Hitachi HF2000 cold FEG operating at 200 kV at the Max-Planck-Institut für Kohlenforschung. Samples were prepared by depositing the powder on a copper TEM grid with an amorphous carbon support film. The particles were measured using ImageJ with a count of at least 150–200 nanoparticles (NPs) to calculate the NP size.

- X-ray Photoelectron Spectroscopy measurements were performed on Ru@SILP$_{AC}$ to identify the electronic structure of the material. Ru@SILP$_{AC}$ after catalysis was also analyzed similarly for comparison. In all cases, the corresponding powder samples were spread onto a carbon tape on the sample holder in a compact manner. XPS measurements were conducted employing a near ambient pressure (NAP) XPS at ultra-high vacuum conditions (~10^{-8} mbar). The system was equipped with an Al-Kα source, which produces monochromated X-rays of energy 1486.6 eV, and a NAP hemispherical energy analyzer with an inbuilt double delay line detector. All high-resolution spectra were recorded using a pass energy of 20 eV and a resolution of 0.05

eV, whereas the survey scans were recorded using 100 eV pass energy. In each case, at least 10 consecutive scans were performed. Data analysis was performed using the CasaXPS software after a binding energy calibration using the C1s at 284.6 eV.[1]

- The Ru K-edge XAS data of the Ru@SILP$_{AC}$ samples (fresh and spent Ru@SILP$_{AC}$ catalysts) were collected at the P65 beamline of PETRA III (P65 Applied X-ray Absorption Spectroscopy).[2] At P65 beamline, a monochromatic beam was introduced through an 11-periods undulator and a Si (311) double crystal monochromator (DCM) with energy resolution $\Delta E/E$ of 6.0×10^{-5}. The DCM was operated in QEXAFS mode, and the undulator offset to the DCM was calibrated to have the maximum photon flux. The beam size at the sample was approx. 0.5 x 1.0 mm^2 (V x H) and the photon flux was ~10^{11} photons/s (without attenuation). The XAFS spectra for all samples were collected in transmission mode, and the intensity of incident beam (I_0) and the transmitted beam (I_t) was monitored by ionization chambers (filled with a mixture of Ar and N_2). The energy range for the full XAFS spectra collected was 21972-22967 eV (k_{max} = 14.5) with energy step sizes of 0.3 eV. The XAFS of each sample was measured 3 times and merged to improve the signal-to-noise ratio. Ru foil was measured simultaneously for each sample as the reference for energy calibration. The energy of the incident beam was calibrated by assigning the energy of the first inflection in the first derivative XANES of Ru foil to 22117 eV. In addition to Ru foil, commercial RuO_2 powder was also measured in transmission mode as a reference. The Ru K-edge XAS spectra were analyzed using the Demeter software package (including Athena and Artemis programs, version 0.9.26).[3] Pre-edge background subtraction and post-edge normalization of the XAFS data were performed using the Athena program. A linear regression background in the range of 21951 to 22046 eV) was determined, and a quadratic polynomial regression for post-edge normalization in the range of 22227 to 22926 eV was applied. The spectra were splined from k=0 to 14.5 Å^{-1} with rbkg of 1.0 Å and *k*-weight of 2. The fitting of EXAFS spectra (R range: 1 to 3 Å, *k*-range: 3.2 to 11.5 Å^{-1}) was performed using the Artemis program based on scattering paths generated from FEFF6. The amplitude reduction factor S_0^2 is determined to be 0.70 by fitting of k^2-weighted R-space EXAFS of Ru foil based on the standard crystal parameters of Ruthenium metal (data from Crystal Open Database, entry ID: 9008513), and was used as fixed parameter for the EXAFS fitting of other Ru samples.

4. Synthesis

4.1. Synthesis and characterization of [3-(4-aminophenethyl)-1-butyl-1H-imidazol-3-ium]Br (IL)

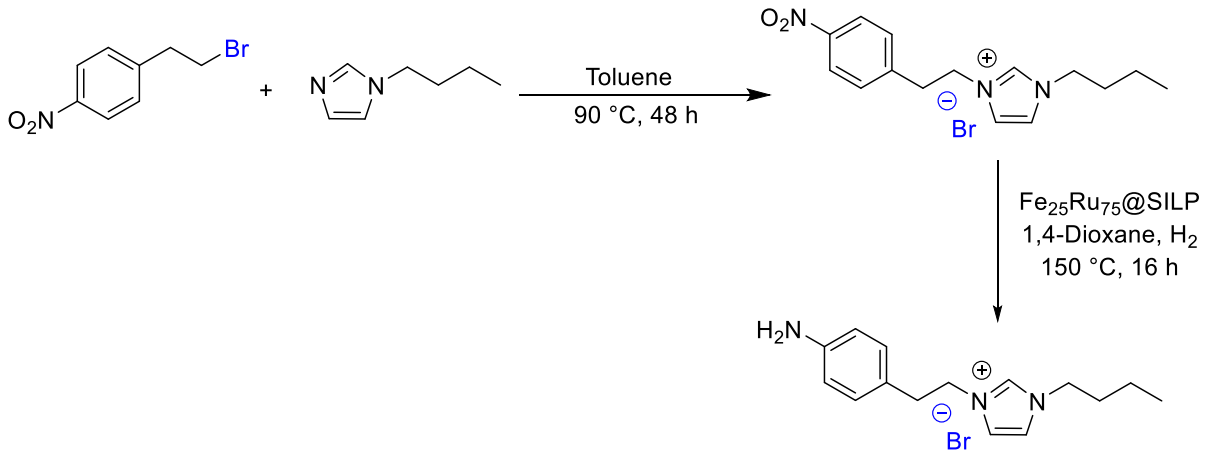

Scheme S1. Synthetic scheme followed for the synthesis of IL.

4.1.1. Synthesis of [1-butyl-3-(4-nitrophenethyl)-1H-imidazol-3-ium]Br

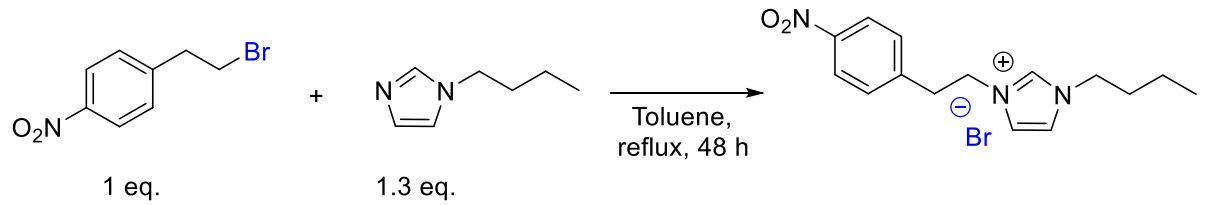

4-Nitrophenylethyl bromide (2 g, 8.6 mmol, 1.0 eq.) was transferred to a round bottom flask and anhydrous toluene (30 mL) was added. Then, 1-butyl imidazole (1.4 g, 11.1 mmol, 1.3 eq.) was added slowly. This reaction mixture was stirred at 90 °C for 48 h. The reaction mixture was cooled down to room temperature, was washed with heptane (3x 10 mL) to remove excess of 1-butyl imidazole, and dried under vacuum to obtain a viscous yellow oil (2.32 g, 6.54 mmol 85% yield).

^{1}H-NMR (400 MHz, CD_3CN): δ (ppm) = 8.36 (s, 1H), 7.99 (m, 2H), 7.32 (m, 2H), 7.24 (m, 2H), 4.44 (t, 2H), 3.93 (t, 2H), 3.19 (t, 2H), 1.53 (m, 2H), 0.87 (m, 2H), 0.66 (m, 3H).

^{13}C-NMR (100.6 MHz, CD_3CN): δ (ppm) = 136.18 (s, 1C), 130.65 (s, 3C), 123.71 (s, 3C), 122.36 (s, 2C), 49.71 (s, 1C), 49.22 (s, 1C), 35.42 (s, 1C), 31.50 (s, 1C), 18.89 (s, 1C), 12.66 (s, 1C).

4.1.2. Synthesis of [3-(4-aminophenethyl)-1-butyl-1H-imidazol-3-ium]Br

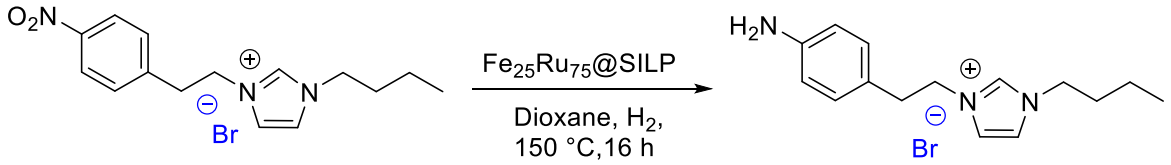

[1-butyl-3-(4-nitrophenethyl)-1H-imidazol-3-ium]Br (1 g, 2.8 mmol) was weighed in a glass inlet and transferred inside a glovebox. To this glass inlet, dry and degassed 1,4-dioxane (2 mL) was added. The $Fe_{25}Ru_{75}$@SILP[4-6] catalyst (40 mg, 0.016 mmol metal loading) was added to this solution, and the inlet was transferred into an autoclave. After properly closing the autoclave, it was brought outside glovebox and pressurized with H_2 (50 bar). The mixture was stirred at 150 °C for 16 h. After reaction, the autoclave was cooled to room temperature and carefully vented. The [3-(4-aminophenethyl)-1-butyl-1H-imidazol-3-ium]Br was extracted with water and filtered off from the solid catalyst under air. Then the solvent was evaporated under reduced pressure giving a thick red oil as [3-(4-aminophenethyl)-1-butyl-1H-imidazol-3-ium]Br (0.74 g, 2.2 mmol, 81% yield).

^{1}H-NMR (400 MHz, CD_3CN): δ (ppm) = 8.68 (s, 1H), 7.347(m, 2H), 6.85 (m, 2H), 6.57 (m, 2H), 4.34 (t, 2H), 4.09 (t, 2H), 2.98 (t, 2H), 1.73 (m, 2H), 1.22 (m, 2H), 0.91 (m, 3H).

^{13}C-NMR (100.6 MHz, CD_3CN): δ (ppm) = 135.79 (s, 1C), 129.42 (s, 3C), 122.46 (s, 2C), 114.69 (s, 3C), 51.02 (s, 1C), 49.15 (s, 1C), 35.02 (s, 1C), 31.62 (s, 1C), 18.90 (s, 1C), 12.73 (s, 1C).

HRMS/ESI(+) (CH_2Cl_2 + CH_3CN): m/z = $[C_{15}H_{22}N_3]^+$ = 244.180821 and $[Br]^-$ = 78.918900

4.2. Synthesis of 1-(4-nitrophenethyl)-1H-imidazole

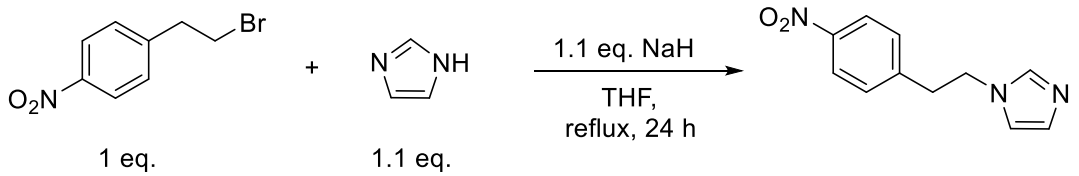

Imidazole (3.2 g, 47.8 mmol, 1.1 eq.) was transferred to a 100 mL Schlenk flask and dry THF (40 mL) was added to the flask. Pentane-washed NaH (1.1 g, 47.8 mmol, 1.1 eq.) was added slowly to the reaction mixture. After stirring the solution for 1 h at room temperature, 3,4-nitrophenylethylbromide (10 g, 43 mmol, 1.0 eq.) was added to this solution and the resulting mixture was stirred under reflux at 90 °C for 24 h. After cooling down to room temperature,

the reaction mixture was filtered and the solid was washed with THF (4 x 20 mL). A yellow viscous liquid was obtained as a crude product after removing solvent under reduced pressure. It was dissolved in DCM (30 mL) and the DCM phase was washed with water to remove unreacted sodium imidazole. The obtained crude product was washed with ether to remove the side product (1-nitro-4-vinylbenzene), followed by drying under vacuum for 24 hours giving a viscous yellow oil as the final product (2.2 g, 10.32 mmol, 24% yield).

^{1}H NMR (400 MHz, CD_3CN): δ(ppm) = 8.12 (d, 2H), 7.32 (d, *J* = 8.6 Hz, 2H), 7.30 (s, 1H), 6.98 (s, 1H), 6.88 (s, 1H), 4.25 (t, *J* = 7.0 Hz, 2H), 3.18 (t, *J* = 7.0 Hz, 2H).

^{13}C NMR (101 MHz, CD_3CN): δ (ppm) = 146.96 (s, 2H), 137.73 (s, 1H), 130.40 (s, 2H), 129.27 (s, 1H), 124.06, (s, 2H), 119.56 (s, 1H), 47.58 (s, 2H), 37.32 (s, 2H).

4.3. Synthesis of 1-(4-nitrophenethyl)-1H-imidazole

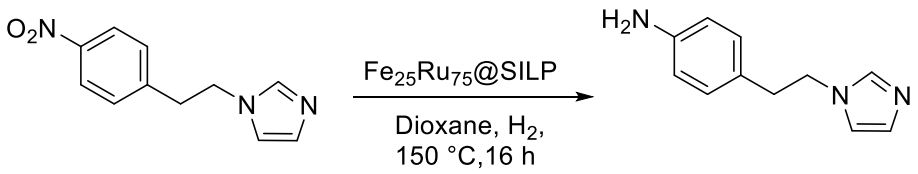

1-(4-nitrophenethyl)-1H-imidazole (1 g, 4.5 mmol) was weighed in a glass inlet and then transferred inside a glovebox. Dry and degassed 1,4-dioxane (1.5 mL) was added. The $Fe_{25}Ru_{75}$@SILP catalyst (40 mg, 0.016 mmol metal loading) was added to this solution. The inlet was transferred into an autoclave, and after properly closing autoclave it was brought outside of the glovebox and pressurized with H_2 (50 bar). The mixture was stirred at 150 °C for 16 h. After reaction, the autoclave was cooled to room temperature and carefully vented. The product was extracted with water and filtered off from the solid catalyst (0.7 g, 3.7 mmol, 82% yield).

^{1}H NMR (400 MHz, CD3CN-*d_3*): δ (ppm) = 7.28 (s, 1H), 6.95 (s, 1H), 6.86 (s, 2H), 6.82 (s, 1H), 6.53 (s, 2H), 4.10 (s, 2H), 2.88 (s, 2H).

^{13}C NMR (101 MHz, CD_3CN): δ (ppm) = 147.13 (s, 1H), 137.72 (s, 1H), 129.88 (s, 2H), 128.96 (s, 1H), 127.19 (s, 1H), 119.59 (s, 1H), 117.91(s, 1H), 115.05 (s, 1H), 48.76 (s, 1H), 36.87 (s, 1H).

4.4. Synthesis of $SILP_C$

4.4.1. General synthetic procedure for $SILP_C$

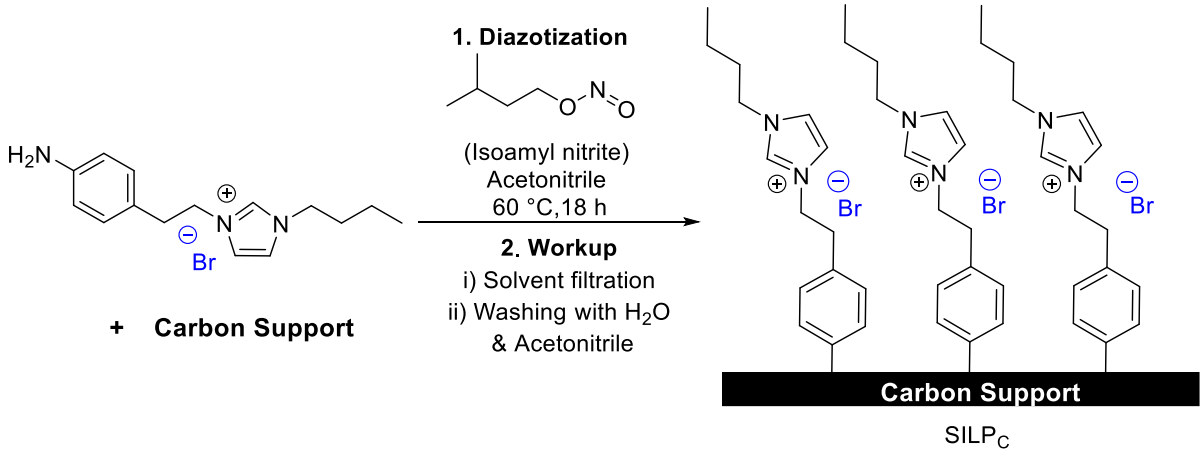

The IL-modified carbon supports ($SILP_C$) were prepared by following a previously reported diazotization method for small organic molecules.[7, 8] Carbon support and IL (Exact amounts are given in specific procedures; sec 4.4.2 – 4.4.6) were introduced in a 500 mL Schlenk flask and dried under vacuum for 4 h to remove any trace of water from support. The Schlenk flask was transferred inside a glovebox and acetonitrile was added, followed by addition of isoamylnitrite (2 eq. to IL). During the addition of isoamyl nitrile, the box light was kept off and the Schenk flask was completely covered with aluminum foil to avoid the exposure of the reaction mixture to light. Keeping it properly covered with foil, the Schenk flask was brought outside the glovebox. Under inert conditions, the reaction mixture was stirred for 18 h at 60 °C, 700 rpm. After cooling the reaction mixture, the black powder was washed five times with acetonitrile, five times with water, and then twice with acetonitrile to remove non-grafted IL. $SILP_C$, as a black solid, was dried in an oven at 60 °C for 4 hours, followed by its drying under vacuum overnight. The filtrates (acetonitrile + water + non-grafted IL) were collected, combined, and evaporated under reduced pressure. The unreacted IL remained in the flask, which was then quantified by ^{1}H-NMR using 1,4-dioxane (39.6 mg, 0.45 mmol) as an internal standard. The IL loading was calculated as the amount of grafted IL per gram of support (mmol.g^{-1}).

Formula **(1)** IL loading = amount of grafted IL/support mass, in mmol g^{-1}

Amount of grafted IL = Initial amount of IL used in synthesis of $SILP_C$ - IL recovered after washing (in mmol)

Formula (**2**): Grafting efficiency = (amount of grafted IL/amount of IL introduced) x 100 %

4.4.2. Synthesis of $SILP_C$ with carbon nanotubes, graphite, and AC

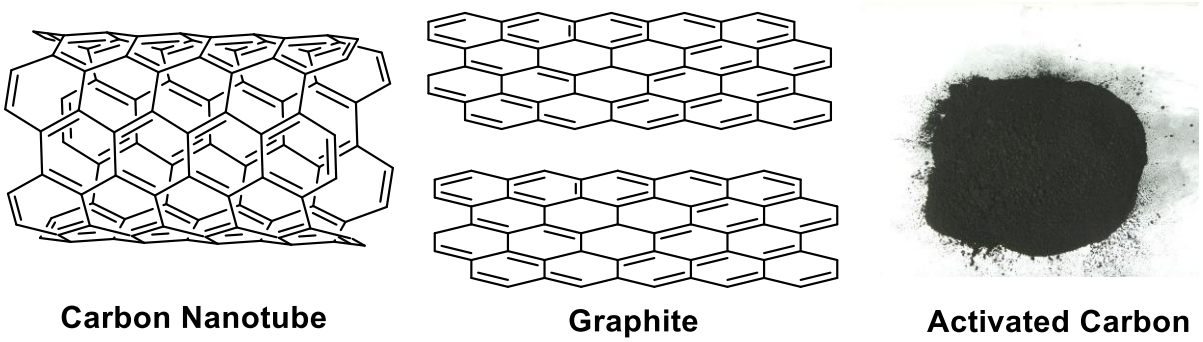

Following the general synthetic procedure discussed in section 4.4.1., $SILP_C$ has been synthesized with different supports, including carbon nanotubes (CNT), graphite, and AC. Carbon Support (1 g), IL (1 g, 3 mmol), and 72 mL of dry acetonitrile were used for synthesis. To the reaction mixture, isoamylnitrite (700 mg, 6 mmol, 2 eq. of IL) was added. IL loading and grafting efficiencies for these supports were calculated using the formula given in section 4.4.1. All results are summarized in Table S1.

4.4.3. Tunability of $SILP_{AC}$ synthesis

Following the general synthetic procedure described in section 4.4.1., $SILP_{AC}$ materials with different amounts of grafted IL have been synthesized simply by varying the weight ratios of IL to AC during synthesis. Exact amounts used for synthesis are provided in Table S2. In all the cases the IL amount has been varied keeping the amount of AC constant, which resulted in the synthesis of $SILP_{AC}$ with varied IL loadings. In all the cases, reproducibility is within ±6% error.

4.4.4. Reproducibility of $SILP_{AC}$ synthesis

Following the general synthetic procedure described in Section 4.4.1, $SILP_{AC}$ was synthesized multiple times at the same scale, and grafting efficiencies were systematically evaluated. Additionally, $SILP_{AC}$ was prepared using different batches of AC from the same supplier (Nuchar), as well as from other suppliers, including Sigma Aldrich, TCI, and Nuchar. The IL loading and grafting efficiencies for these various supports were determined using the

calculation method described in section 4.4.1. The values of starting materials used and grafting efficiency results are given in Table S3 and S4.

4.4.5. Scalability of $SILP_{AC}$ synthesis

Following the general synthetic procedure described in section 4.4.1., $SILP_{AC}$ materials with varying scales ranging from 0.1 g – 2 g have been synthesized. The amounts of substrates, solvents, and grafting efficiencies are provided in Table S5. IL loadings and grafting efficiencies for these supports were calculated using the method presented in section 4.4.1.

4.4.6. Stability of $SILP_{AC}$

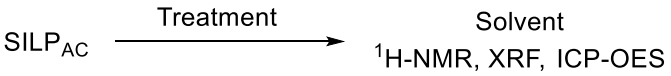

$SILP_{AC}$ (500 mg) was thoroughly washed with water and acetonitrile (IL is soluble in H_2O and acetonitrile). All the washing solutions were collected in a flask, and the solvents were evaporated under reduced pressure, so that only leached IL would remain in the flask. In the same flask, 1 mL of acetonitrile and 1,4-dioxane (39.6 mg, 0.45 mmol) as internal standard were added, and the mixture was analyzed by ^{1}H-NMR (Figure S3), XRF, and ICP-OES (Br, characteristics of IL) (Table S6) for determining the IL leaching. All these analytics indicated no leaching of IL.

In addition, to test the stability of $SILP_{AC}$ under elevated temperature and pressure, 100 mg of $SILP_{AC}$ was heated at 100 °C under 60 bar hydrogen in 2 mL D_2O for 24 hours. After cooling 1,4-dioxane was added to the solution as an internal standard. The solution was analyzed by ^{1}H-NMR (Figure S3), XRF, ICP-OES (Table S6), which indicated no leaching of IL (Figure S3).

Similarly, $SILP_{AC}$ (500 mg) has been treated with toluene to wash off IL potentially immobilized on AC via *pi* interactions. It was also washed with acetonitrile and water. All the washing solutions were collected in a flask, and solvents were evaporated under reduced pressure, so that only leached IL would remain in the flask. In the same flask, 1 mL of acetonitrile and 1,4-dioxane (39.6 mg, 0.45 mmol) as internal standard were added, and analyzed by ^{1}H-NMR (Figure S3), XRF, and ICP-OES (Br, characteristics of IL) (Table S6) for determining the IL leaching. All these analytics showed no characteristics of IL.

4.5. Synthesis of AC(Imz)

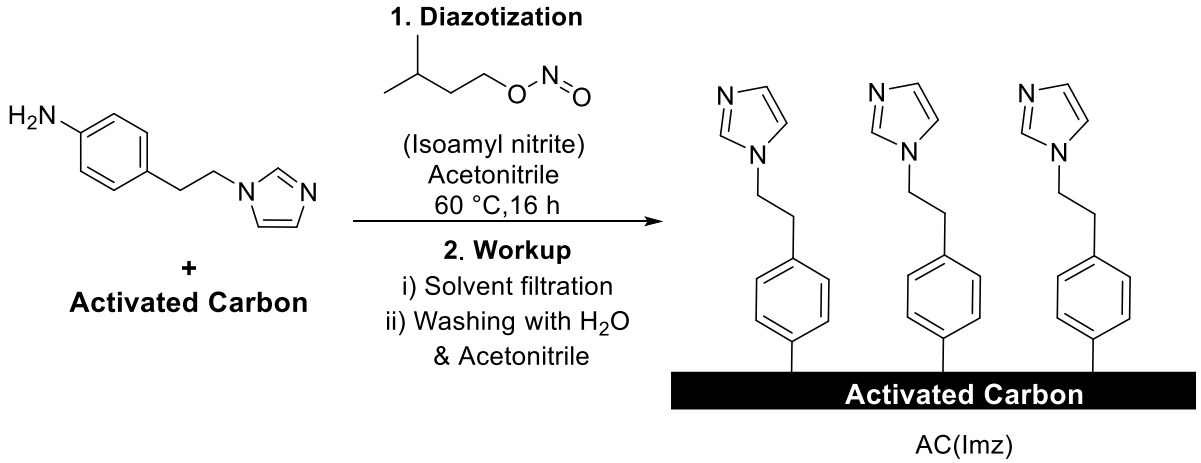

Following the general synthetic procedure discussed in section 4.4.1., AC(Imz) was synthesized using AC (500 mg), 4-(2-(1H-imidazol-1-yl)ethyl)aniline (136 mg, 0.73 mmol) and isoamylnitrite (360 mg, 1.46 mmol, 2 eq.). The loading of the organic moiety (Imz) on AC was determined as 1.2 mmol.g^{-1}.

4.6. Synthesis of Ru@SILP$_{AC}$

4.6.1. General procedure for the synthesis of Ru@Support

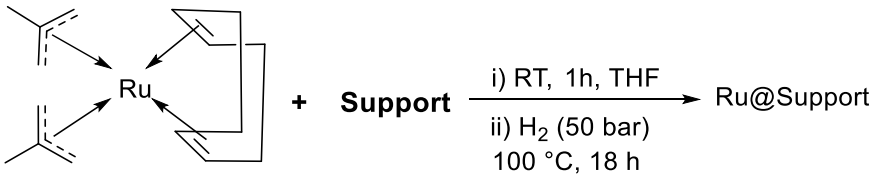

The immobilization of Ru NPs on the different support materials was accomplished by following a reported procedure by our group.[6] The support (1 g) was weighed in a 250 mL dry Schlenk flask and kept under vacuum for 2 hours to remove any trace of water. The Schlenk flask was transferred into the glovebox. In a glass vial, a solution of [Ru(2-methylallyl)$_2$(cod)] (35.0 mg, 0.1 mmol) in THF (30 mL) was prepared and added to the Schlenk flask, and the mixture was stirred for 1 hour at room temperature under Ar atmosphere outside the glovebox. After evaporating the solvent under vacuum, the impregnated powder was transferred to a glass inlet, which was then pressurized with H_2 (50 bar) and heated at 100 °C for 18 h. After cooling the reaction to room temperature, pressure was released slowly, and prepared catalysts were stored outside the glovebox.

Determination of Ru surface atoms:

Assumptions considered for the calculation of the surface Ru:

1. All particles are considered spherical and the distribution of surface Ru atoms on the surface is symmetric in all directions.

2. The contribution from size distribution is not considered.

3. The surface is considered to be purely metallic without any oxidation or coordination from any ligands.

4. The body volume of the NPs is filled with Ru atoms in hcp structure, while all surface volumes are filled with Ru atoms in closed-packed approximation.

The %(surface Ru) was estimated for each catalyst by calculating volume of Ru NPs as well as volume of the shell containing first layer of Ru atoms.

The volume of nanoparticles:

$$V_{NPs} = 4/3\ \pi \times r^3{}_{NPs}$$

The volume of the shell containing first layer of ruthenium atoms

$$V_{\text{shell}} = \ 4/3\ \pi \times (r^3{}_{NPs} - (r_{NPs} - \ r_{at(Ru)})^3)$$

With atomic radius of the Ru ($r_{at(Ru)}$) = 0.13 nm.

$$\%_{Surface\ Ru} = \frac{Vshell}{VNPs}$$

For all the synthesized catalysts results are summarized in Table S7.

4.6.2. Synthesis of Ru@AC+IL$_1$

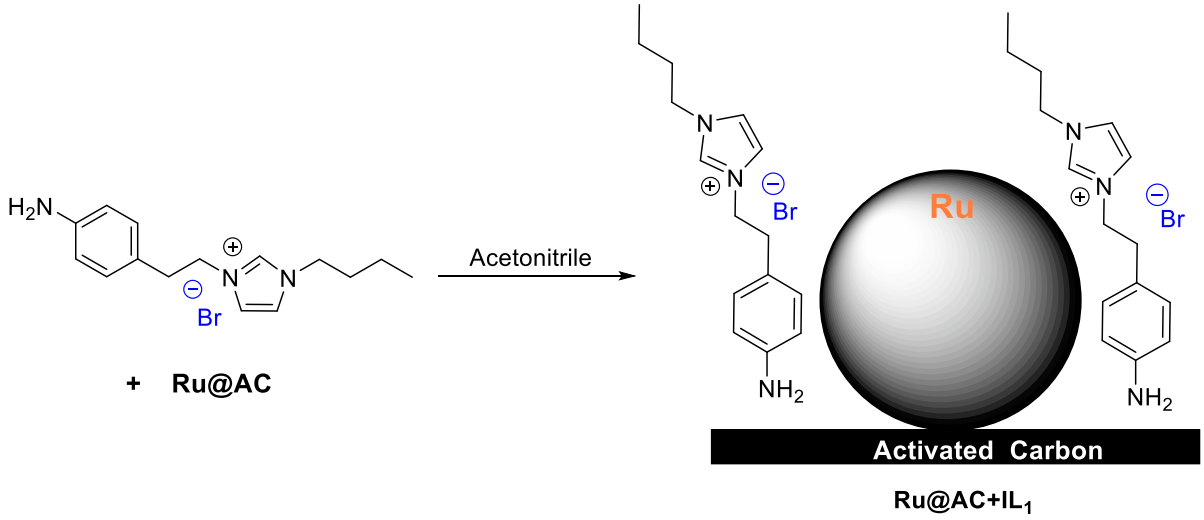

A 200 mL round-bottom flask was loaded with 500 mg of Ru@AC, followed by the addition of IL ([3-(4-aminophenethyl)-1-butyl-1H-imidazol-3-ium]Br) (178 mg, 0.55 mmol, corresponding to a loading of 1.1 mmol.g^{-1} for SILP$_{AC}$). To this mixture, 36 mL of acetonitrile was added, and the reaction was stirred at room temperature overnight. The solvent was subsequently removed under vacuum, yielding the Ru@AC+IL$_1$.

4.6.3. Synthesis of Ru@AC+IL$_2$

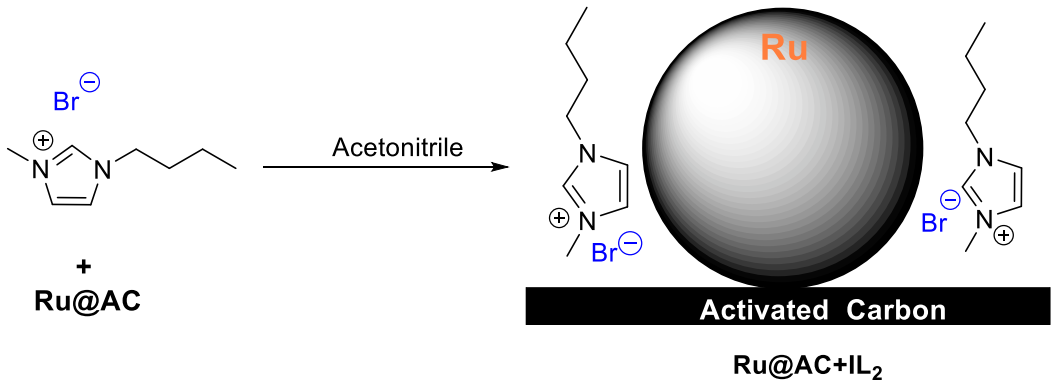

A 200 mL round-bottom flask was loaded with 500 mg of Ru@AC, followed by addition of IL (1-butyl-3-methylimidazolium bromide) (120 mg, 0.55 mmol, corresponding to a loading of 1.1 mmol.g^{-1} for SILP$_{AC}$). To this mixture, 36 mL of acetonitrile was added, and the reaction was stirred at room temperature overnight. The solvent was subsequently removed under vacuum, yielding the Ru@AC+IL$_2$.

4.6.4. Synthesis of Ru@AC(Imz)

General synthetic procedure given in section 4.6.1. has been used for the synthesis of Ru@AC(Imz). AC_{Imz} (500 mg), prepared in section 4.5. was used as support.

5. Catalytic study

5.1. General procedure for the hydrogenation of CO_2

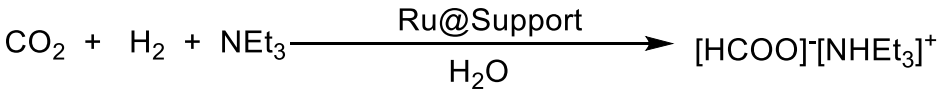

In a typical experiment, Ru@Support (50 mg, 0.005 mmol Ru, theoretical), triethylamine (0.55 mL, 3.95 mmol), and water (0.75 mL, 41 mmol) were added to a glass inlet and transferred inlet to a high-pressure autoclave under air. The reaction mixture was stirred at the desired temperature in an aluminum heating block under a mixture of CO_2 + H_2 (1:2 ratio, 60 bar total pressure). At the end of reaction, reactor was cooled and carefully vented. The gas phase was analysed by GC-TCD/FID, and reaction solution by ^{1}H NMR using 1,4-dioxane as a standard.

Turnover numbers were determined using following equation:

$$TON = \frac{nformate}{nRu * \%Surface\ Ru}$$

5.2. Procedure for studying time profile of formic acid decomposition using Ru@SILP$_{AC}$ and Ru@AC

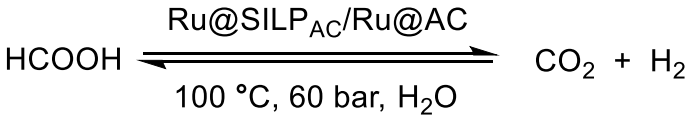

To investigate the time profile for decomposition of formic acid, independent batch experiments were performed at different reaction times. This process continued until the system reached equilibrium. In a typical procedure, 0.75 mL of a 0.2 M aqueous solution of formic acid was transferred into a glass inlet. Subsequently, Ru@SILP$_{AC}$/Ru@AC catalyst (50 mg, corresponding to 0.005 mmol of Ru, theoretical) was added. The glass inlet was then placed inside a high-pressure autoclave under an air atmosphere. The reactor was sealed and pressurized with a gas mixture of CO_2 and H_2 (1:2 ratio) to a total pressure of 60 bar. The

reaction mixture was stirred at 100 °C using an aluminum heating block for the desired reaction time (t = 1 h, 3 h, 5 h, 24 h, and 42 h). After completion of reaction, autoclave was allowed to cool to room temperature and was vented carefully. The amount of formic acid remaining in the reaction solution was quantified by ^{1}H NMR spectroscopy, using 1,4-dioxane as an internal standard. Freshly prepared reaction mixtures were used for each time point to ensure reproducibility.

5.3. Procedure for studying time profile of hydrogenation of CO_2 to formic acid using Ru@SILP$_{AC}$ and Ru@AC

$$CO_2 + H_2 \underset{100\ °C,\ 60\ bar,\ H_2O}{\overset{Ru@SILP_{AC}/Ru@AC}{\rightleftharpoons}} HCOOH$$

To investigate the time profile for synthesis of formic acid, independent batch experiments were performed at different reaction times. This process continued until the system reached equilibrium. In a typical procedure, 0.75 mL of water was transferred into a glass inlet. Subsequently, Ru@SILP$_{AC}$/Ru@AC catalyst (50 mg, corresponding to 0.005 mmol of Ru, theoretical) was added. The glass inlet was then placed inside a high-pressure autoclave under an air atmosphere. The reactor was sealed and pressurized with a gas mixture of CO_2 and H_2 (1:2 ratio) to a total pressure of 60 bar. The reaction mixture was stirred at 100 °C using an aluminum heating block for the desired reaction time (t = 1 h, 6 h, 24 h, and 42 h). After completion of reaction, autoclave was allowed to cool to room temperature and vented carefully. The amount of formic acid produced in reaction solution was quantified by ^{1}H NMR spectroscopy, using 1,4-dioxane as an internal standard. Freshly prepared reaction mixtures were used for each time point to ensure reproducibility.

5.4. Procedure for studying time profile of triethylammonium formate decomposition using Ru@SILP$_{AC}$ and Ru@AC

$$[HCOO]^-[NHEt_3]^+ \underset{T\ °C,\ 60\ bar,\ H_2O}{\overset{Ru@SILP_{AC}/Ru@AC}{\rightleftharpoons}} CO_2 + H_2 + NEt_3$$

To investigate the time profile for the decomposition of triethylammonium formate, independent batch experiments were performed at different reaction times. This process continued until the system reached equilibrium. In a typical procedure, 0.75 mL of a 5.2 M aqueous solution of formic acid was transferred into a glass inlet, followed by addition of

triethylamine (0.55 mL, 3.95 mmol, 1 eq. to formic acid), and then the reaction mixture was stirred at room temperature for 1 hour to ensure the formation of triethylammonium formate. After stirring, Ru@SILP$_{AC}$/Ru@AC catalyst (50 mg, corresponding to 0.005 mmol of Ru, theoretical) was added. The glass inlet was then placed inside a high-pressure autoclave under an air atmosphere. The reactor was sealed and pressurized with a gas mixture of CO_2 and H_2 (1:2 ratio) to a total pressure of 60 bar. The reaction mixture was stirred at 100 °C using an aluminum heating block for the desired reaction time (t = 1 h, 4 h, 20 h, and 40 h). After completion of reaction, the autoclave was allowed to cool to room temperature and vented carefully. The amount of triethylammonium formate remaining in reaction solution was quantified by ^{1}H NMR spectroscopy, using 1,4-dioxane as an internal standard. Freshly prepared reaction mixtures were used for each time point to ensure reproducibility.

A similar study for decomposition of triethylammonium formate has been performed at different conditions for which the amounts of reactants, solvent, catalysts, and temperature are provided in Table S9.

5.5. Procedure for studying time profile of hydrogenation of CO_2 to triethylammonium formate decomposition using Ru@SILP$_{AC}$ and Ru@AC

$$CO_2 + H_2 + NEt_3 \underset{T\ °C,\ 60\ bar,\ H_2O}{\overset{Ru@SILP_{AC}/Ru@AC}{\rightleftharpoons}} [HCOO]^-[NHEt_3]^+$$

To investigate the time profile of hydrogenation of CO_2 to triethylammonium formate, a series of independent batch experiments were conducted at different reaction times. This process continued until the system reached equilibrium. In a typical procedure, triethylamine (0.55 mL, 3.95 mmol), and water (0.75 mL, 41 mmol) were added to a glass inlet. Subsequently, Ru@SILP$_{AC}$/Ru@AC catalyst (50 mg, corresponding to 0.005 mmol of Ru, theoretical) was added. The glass inlet was then placed inside a high-pressure autoclave under an air atmosphere. The reactor was sealed and pressurized with a gas mixture of CO_2 and H_2 (1:2 ratio) to a total pressure of 60 bar. The reaction mixture was stirred at 100 °C using an aluminum heating block for the desired reaction time (t = 1 h, 3 h, 5 h, 12 h, 16 h, 20 h, and 36 h). After completion of reaction, the autoclave was allowed to cool to room temperature and was vented carefully. The amount of triethylammonium formate produced in the reaction solution was quantified by ^{1}H NMR spectroscopy, using 1,4-dioxane as an internal standard. Freshly prepared reaction mixtures were used for each time point to ensure reproducibility.

A similar study for the synthesis of triethylammonium formate has been performed under different conditions for which the amounts of reactants, solvent, catalysts, and temperature are provided in Table S9.

5.6. General procedure for the recycling of Ru@SILP$_{AC}$

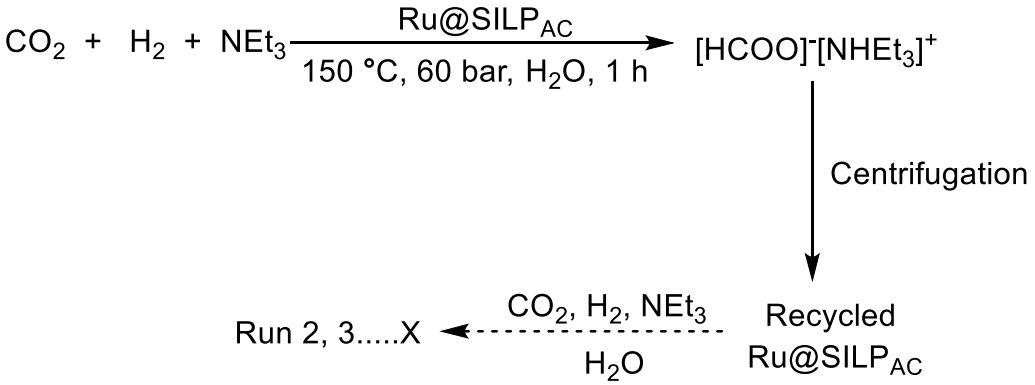

All the catalytic cycle has been performed following the general procedure for hydrogenation of CO_2 given in section 5.1., except reusing the same catalyst for all the cycles. After completing the each catalytic cycle, the autoclave was allowed to cool and was then cautiously vented. The reaction mixture was subjected to centrifugation to separate the Ru@SILP$_{AC}$ catalyst from the solution. The supernatant was carefully decanted, and the catalyst was washed twice with water. The washings were combined with the original reaction solution, and 1,4-dioxane was added to the resulting mixture. The amount of formate produced was then quantified using ^{1}H NMR spectroscopy. The washed catalyst was then used directly for the next cycle without further treatment.

5.7. General procedure for the hydrogenation/dehydrogenation reversibly experiments

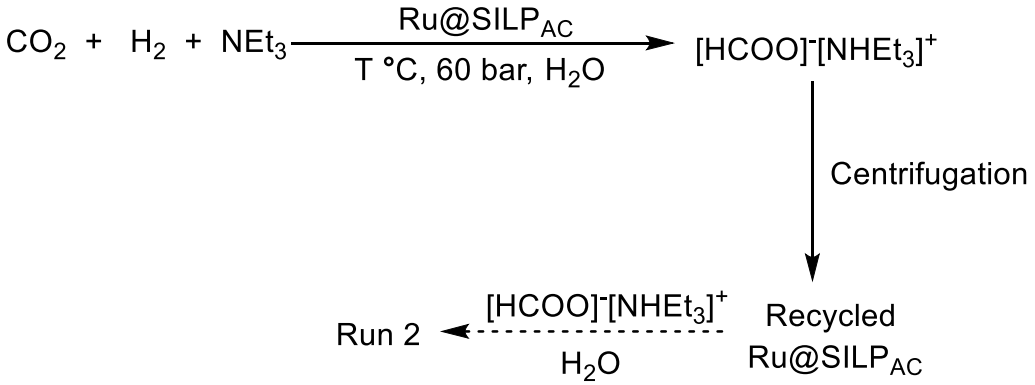

In a typical experiment, Ru@SILP$_{AC}$ (50 mg, 0.005 mmol Ru, theoretical), triethylamine (0.55 mL, 3.95 mmol), and water (0.75 mL, 41 mmol) were added to a glass inlet and

transferred inlet to a high-pressure autoclave under air. The reaction mixture was stirred at the desired temperature in an aluminum heating block under a mixture of CO_2 + H_2 (1:2 ratio, 60 bar total pressure). At the end of reaction, reactor was cooled and carefully vented. The reaction mixture was subjected to centrifugation to separate the Ru@$SILP_{AC}$ catalyst from the solution. The supernatant was carefully decanted, and the catalyst was washed twice with water. The washings were combined with the original reaction solution, and 1,4-dioxane was added to the resulting mixture. The amount of formate produced was then quantified using ^{1}H NMR spectroscopy.

The washed Ru@$SILP_{AC}$ catalyst was then reused directly in the subsequent dehydrogenation experiment without further treatment. For the dehydrogenation step, the reaction solution (containing the in situ generated triethylammonium formate) was transferred into the same glass inlet containing the recycled catalyst. The mixture was again stirred at the desired temperature in an aluminum heating block. The gas phase was released and analysed by GC-TCD/FID after every two hours. After completion of the reaction, the reaction mixture was subjected to centrifugation to separate the Ru@$SILP_{AC}$ catalyst from the solution. The supernatant was carefully decanted, and the catalyst was washed twice with water. The washings were combined with the original reaction solution, and 1,4-dioxane was added to the resulting mixture. The amount of formate left was then quantified using ^{1}H NMR spectroscopy. The recovered catalyst was reused directly in the next hydrogenation–dehydrogenation cycle without any further processing.

5.8. Scaling up the hydrogenation of CO_2 to formate with Ru@$SILP_{AC}$

Ru@$SILP_{AC}$ (50 mg, 0.00179 mmol Ru), triethylamine (58 mL, 416 mmol), and water (22 mL, 1.222 mol) were introduced in a 100 mL high-pressure reactor under air. The reaction mixture was heated at 150 °C using an electrical heater under a mixture of CO_2 + H_2 (1:2 ratio, 60 bar total pressure) with mechanical stirring at 1000 rpm. At the end of the reaction, the reactor was cooled and carefully vented. The catalyst was removed by passing the reaction solution through a syringe filter, and triethylammonium formate was quantified by ^{1}H NMR using 1,4-dioxane as a standard.

6. Supplementary tables

Table S1. Characterization of carbon support materials and corresponding SILPs.

Support	IL loading[a] (mmol.g^{-1})	Grafting efficiency[b](%)	Surface area (m^2/g)
AC	-	-	2840
Graphite	-	-	160
CNTs	-	-	296
$SILP_{AC}$	2.2	73	1101
$SILP_{Graphite}$	1.0	33	-
$SILP_{CNTs}$	1.4	46	171

[a]Determined based on formula (1); [b]determined based on formula (2) given in section 4.4.1.

Table S2. Variation of IL loading on $SILP_{AC}$.

$SILP_{AC}$ (g)	IL added (mmol)	Experimental IL loading[a] (mmol.g^{-1})	Grafting efficiency[b] (%)	Br loading [wt%]
0.5	0.38	0.55	72	1.08
=	0.61	0.83	81	2.30
=	0.73	1.1	75	2.84
=	1.09	1.7	78	2.77
=	1.54	2.4	78	4.04

Reaction conditions: AC (500 mg), isoamylnitrite (2 eq. to IL), IL (xx mmol) and acetonitrile (36 mL), 18 h at 60 °C, 700 rpm; [a]determined based on formula (1); [b]determined based on formula (2) given in section 4.4.1.

Table S3. Batch-to-batch reproducibility for the synthesis of $SILP_{AC}$ using commercial AC from Nuchar.

Entry	AC batch	Experimental IL Loading[a] ($mmol.g^{-1}$)	Grafting efficiency[b] (%)
1	Batch 1	2.4	78
2	Batch 1	2.1	70
3	Batch 1	2.2	73
4	Batch 2	2.0	66

Reaction conditions: AC (500 mg), IL (500 mg, 1.54 mmol, 1 eq.), isoamylnitrite (360 mg, 3.08 mmol, 2 eq.) and acetonitrile (36 mL), 18 h, 60 °C, 700 rpm; [a]determined based on formula (1); [b]determined based on formula (2) given in section 4.4.1.

Table S4. Batch-to-batch reproducibility for the synthesis of $SILP_{AC}$ using commercial AC from different suppliers.

Entry	AC supplier	Experimental IL Loading[a] ($mmol.g^{-1}$)	Grafting efficiency[b] (%)
1	Nuchar	2.4	78
2	TCI	1.9	63
3	Sigma Aldrich	2.0	68

Reaction conditions: AC (500 mg), IL (500 mg, 1.54 mmol, 1 eq.), isoamylnitrite (360 mg, 3.08 mmol, 2 eq.) and acetonitrile (36 mL), 18 h at 60 °C, 700 rpm; [a]determined based on formula (1); [b]determined based on formula (2) given in section 4.4.1.

Table S5. Scalability in the preparation of $SILP_{AC}$.

Entry	AC (g)	IL added (mmol)	Solvent (mL)	IL loading[a] ($mmol.g^{-1}$)	Grafting efficiency[b] (%)
1	0.1	0.3	6	2.2	73
2	0.5	1.5	36	2.4	78
3	1	3.1	72	2.3	74
4	2	6.2	144	2.4	77

Reaction conditions: Isoamylnitrite (2 eq. to IL), 18 h at 60 °C, 700 rpm; [a]determined based on formula (1); [b]determined based on formula (2) given in section 4.4.1.

Table S6. IL leaching (represented by Br) in $SILP_{AC}$ washing solutions as characterized by XRF and ICP-OES.

Washing conditions	Br leaching (%)	
	XRF	ICP-OES
Treatment with H_2O and ACN at 25 °C for 2 h	1.7 %	2.3 %
Heating at 100 °C + 60 bar H_2 in D_2O for 24 h	1.4 %	2.5 %
Treatment with Toluene, H_2O and ACN at 25 °C	1.1 %	2.2 %

Table S7. Analytics and characterization data of Ru@Support, as well as data for calculating surface Ru.

Catalyst	Theoretical Ru ($mmol.g^{-1}$)	Exp. Ru Loading ($mmol.g^{-1}$)	Surface area ($m^2.g^{-1}$)	NPs Size (nm)	V_{NPs} (nm^3)	V_{shell} (nm^3)	Surface Ru (%)	Surface Ru ($mmol.g^{-1}$)
Ru@AC	0.1	0.085	2840	1.2 ± 0.3	0.90	0.46	51.8	0.044
$Ru@SILP_{AC}$ (IL:0.5 $mmol.g^{-1}$)	0.1	0.090	1725	1.4 ± 0.3	1.43	0.65	45.9	0.0413
$Ru@SILP_{AC}$ (IL:0.8 $mmol.g^{-1}$)	0.1	0.077	1149	1.3 ± 0.3	1.14	0.56	48.6	0.0379
$Ru@SILP_{AC}$ (IL:1.1 $mmol.g^{-1}$)	0.025	0.021	-	1.7 ± 0.3	2.57	1.00	39.13	0.0082
	0.05	0.051	-	1.3 ± 0.3	1.14	0.56	48.6	0.0243
	0.1	0.081	1282	1.5 ± 0.3	1.76	0.76	43.4	0.0358
	0.15	0.140	-	1.3 ± 0.2	1.14	0.56	48.6	0.0671
$Ru@SILP_{AC}$ (IL:1.7 $mmol.g^{-1}$)	0.1	0.083	1072	1.6 ± 0.3	2.14	0.88	41.1	0.0345
$Ru@SILP_{AC}$ (IL:2.4 $mmol.g^{-1}$)	0.1	0.080	964	1.5 ± 0.3	1.76	0.76	43.4	0.0351

Table S8. Fitting results of Ru K-edge k^2-weighted EXAFS spectra.

Sample	Scattering path	C.N.	R [Å]	σ^2 [Å^2]	E_0 [eV]	R-factor
Ru@AC	Ru-O	1.3 ± 0.4	1.85 ± 0.03	0.0042 ± 0.0010	22125.4 ± 1.4	0.0061
	Ru-O	4.8 ± 0.5	2.01 ± 0.01			
	Ru-Ru	2.7 ± 0.6	2.68 ± 0.01	0.0083 ± 0.0021		
Ru@SILP$_{AC}$	Ru-O	0.9 ± 0.3	1.84 ± 0.04	0.0037 ± 0.0013	22126.2 ± 1.5	0.0161
	Ru-O	3.7 ± 0.5	2.05 ± 0.01			
	Ru-Ru	3.0 ± 0.6	2.69 ± 0.01	0.0048 ± 0.0012		
Ru@SILP$_{AC}$ after catalysis	Ru-O	1.1 ± 0.3	1.84 ± 0.03	0.0046 ± 0.0006	22124.8 ± 0.8	0.0050
	Ru-O	3.4 ± 0.3	2.05 ± 0.01			
	Ru-Ru	5.0 ± 0.5	2.68 ± 0.01	0.0052 ± 0.0008		

Table S9. Reaction conditions and reaction rates reported in Figure 4.

Experiment	Catalyst	T (°C)	Solvent System			Equilibrium position	Rate
			H_2O	NEt_3	HCOOH		
[a]HCOOH decomposition	Ru@SILP$_{AC}$	100	0.75 mL	-	7 mg, 0.15 mmol	14 mmol L^{-1}	0.18 mol L^{-1} h^{-1}
	Ru@AC	100	0.75 mL	-	7 mg, 0.15 mmol	2.7 mmol L^{-1}	0.14 mol L^{-1} h^{-1}
HCOOH formation	Ru@SILP$_{AC}$	100	0.75 mL	-	-		8.6 mmol L^{-1} h^{-1}
	Ru@AC	100	0.75 mL	-	-		2.3 mmol L^{-1} h^{-1}
[b]HCOOH decomposition	Ru@SILP$_{AC}$	100	0.75 mL	0.55 mL, 3.95 mmol	182 mg, 3.95 mmol	72%	0.62 mol L^{-1} h^{-1}
	Ru@AC	100	0.75 mL	0.55 mL, 3.95 mmol	182 mg, 3.95 mmol	68%	0.52 mol L^{-1} h^{-1}
HCOOH formation	Ru@SILP$_{AC}$	100	0.75 mL	0.55 mL, 3.95 mmol	-		0.03 mol L^{-1} h^{-1}

	Ru@AC	100	0.75 mL	0.55 mL, 3.95 mmol	-		0.1 mol L^{-1} h^{-1}
[b]HCOOH decomposition	Ru@SILP$_{AC}$	150	0.22 mL	0.58 mL, 4.1 mmol	188 mg, 4.1 mmol	14%	6 mol L^{-1} h^{-1}
	Ru@AC	150	0.22 mL	0.58 mL, 4.1 mmol	188 mg, 4.1 mmol	8%	8 mol L^{-1} h^{-1}
HCOOH formation	Ru@SILP$_{AC}$	150	0.88 mL	2.32 mL, 16.7 mmol	-		0.03 mol L^{-1} h^{-1}
	Ru@AC	150	0.88 mL	2.32 mL, 16.7 mmol	-		0.2 mol L^{-1} h^{-1}

[a]*Equilibrium position = Concentration of formic acid*

[b]*Equilibrium position = (Amount of formate/Amount of NEt_3)*100*

Table S10. HCOOH formation and decomposition reactions at short times using Ru@SILP$_{AC}$ and Ru@AC.

Experiment	Catalyst	Time	Solvent System			HCOOH/NEt_3 (%)	TOF[a] (h^{-1})
			H_2O	NEt_3	HCOOH		
HCOOH decomposition	Ru@SILP$_{AC}$	15 min	0.75 mL	0.55 mL, 3.95 mmol	182 mg, 3.95 mmol	78	1941
	Ru@SILP$_{AC}$	1 h	0.75 mL	0.55 mL, 3.95 mmol	182 mg, 3.95 mmol	76.4	520
	Ru@AC	15 min	0.75 mL	0.55 mL, 3.95 mmol	182 mg, 3.95 mmol	82	1292
	Ru@AC	1 h	0.75 mL	0.55 mL, 3.95 mmol	182 mg, 3.95 mmol	81.1	339
HCOOH formation	Ru@SILP$_{AC}$	15 min	0.75 mL	0.55 mL, 3.95 mmol	-	1	88
	Ru@SILP$_{AC}$	1 h	0.75 mL	0.55 mL, 3.95 mmol	-	3.5	77
	Ru@AC	15 min	0.75 mL	0.55 mL, 3.95 mmol	-	0.8	57
	Ru@AC	1 h	0.75 mL	0.55 mL, 3.95 mmol	-	1.2	21

Reaction conditions: Ru@SILP$_{AC}$/Ru@AC (50 mg, 1.1 $mmol_{IL}.g^{-1}$, 0.1 $mmol_{Ru}.g^{-1}$ theoretical), 60 bar total pressure with CO_2:H_2 = 1:2, 100 °C. [a]average values of 2-3 experiments based on experimental Ru loading (Ru@AC: 0.085 $mmol_{Ru}.g^{-1}$; Ru@SILP$_{AC}$: 0.081 $mmol_{Ru}.g^{-1}$) and estimated surface Ru atoms (Ru@AC: 0.044 $mmol_{Ru}.g^{-1}$; Ru@SILP$_{AC}$: 0.0358 $mmol_{Ru}.g^{-1}$).

Table S11. Influence of IL loading.

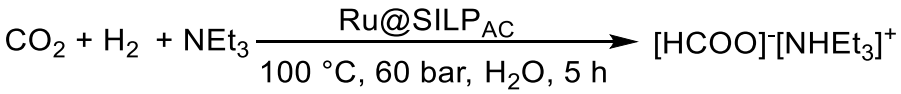

Entry	Catalyst	$Y_{formate}$ [mmol]	Formate/NEt_3 [%]	TON[a]
1	Ru@AC	0.20	5	93
2	Ru@$SILP_{AC}$ (IL:0.5 mmol.g^{-1})	0.32	8	147
3	Ru@$SILP_{AC}$ (IL:0.8 mmol.g^{-1})	0.43	11	227
4	Ru@$SILP_{AC}$ (IL:1.1 mmol.g^{-1})	0.60	15	333
5	Ru@$SILP_{AC}$ (IL:1.7 mmol.g^{-1})	0.40	10	233
6	Ru@$SILP_{AC}$ (IL:2.4 mmol.g^{-1})	0.38	9	198

Reaction conditions: Ru@$SILP_{AC}$ (50 mg, 0.1 $mmol_{Ru}.g^{-1}$ theoretical), 60 bar total pressure with CO_2:H_2 = 1:2, 100 °C, solvent system: NEt_3 (3.95 mmol, 0.55 mL) + H_2O (41 mmol, 0.75 mL), time: 5 h; [a]average values of 2-3 experiments based on experimental Ru loadings and estimated surface Ru atoms given in table S7.

Table S12. Influence of Ru NPs loading.

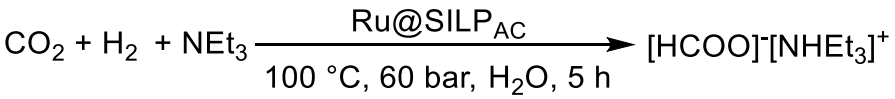

Entry	Theoretical Ru (mmol.g^{-1})	$Y_{formate}$ [mmol]	Formate/NEt_3 [%]	TON[a]
1	0.025	0.02	0.5	42
2	0.05	0.43	8	258
3	0.1	0.60	15	333
4	0.15	0.67	17	256

Reaction conditions: Ru@$SILP_{AC}$ (50 mg, 1.1 $mmol_{IL}.g^{-1}$, x $mmol_{Ru}.g^{-1}$), 60 bar total pressure with CO_2:H_2 = 1:2, 100 °C, solvent system: NEt_3 (3.95 mmol, 0.55 mL) + H_2O (41 mmol, 0.75 mL), time: 5 h; [a]average values of 2-3 experiments based on experimental Ru loadings and estimated surface Ru atoms given in table S7.

Table S13. Influence of temperature.

Entry	Temperature (°C)	$Y_{formate}$ [mmol]	Formate/NEt_3 [%]	TON[a]
1	100	0.12	3	72
2	140	0.45	11	251
3	150	0.60	15	333
4	155	0.45	11	250
5	160	0.40	9	223
6	165	0.33	8	194
7	170	0.16	4	90
8	200	0.01	0.2	6

Reaction conditions: Ru@$SILP_{AC}$ (50 mg, 1.1 $mmol_{IL}.g^{-1}$, 0.1 $mmol_{Ru}.g^{-1}$ theoretical), 60 bar total pressure with CO_2:H_2 = 1:2, X °C, solvent system: NEt_3 (4.1 mmol, 0.58 mL) + H_2O (12 mmol, 0.22 mL), total volume: 0.8 mL, time: 1 h; [a]average values of 2-3 experiments based on experimental Ru loadings (0.081 $mmol_{Ru}.g^{-1}$) and estimated surface Ru atoms (0.0358 $mmol_{Ru}.g^{-1}$).

Table S14. Influence of reaction volume at constant catalyst loading.

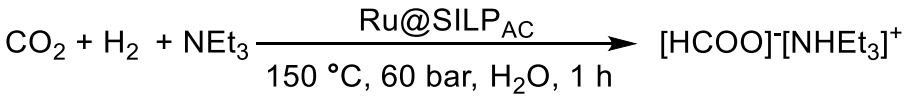

Entry	Volume	$Y_{formate}$ [mmol]	Formate/NEt_3 [%]	TON[a]
1	0.8	0.60	15	333
2	1.6	1.21	14	683
3	2.4	1.57	12	874
4	3.2	1.98	12	1110

Reaction conditions: $Ru@SILP_{AC}$ (50 mg, 1.1 $mmol_{IL}.g^{-1}$, 0.1 $mmol_{Ru}.g^{-1}$ theoretical), 60 bar total pressure with CO_2:H_2 = 1:2, 150 °C, solvent system: NEt_3 (x mmol, x mL) + H_2O (x mmol, x mL), total volume: x mL, NEt_3/H_2O molar ratio = 0.34, time: 1 h; [a]average values of 2-3 experiments based on experimental Ru loadings (0.081 $mmol_{Ru}.g^{-1}$) and estimated surface Ru atoms (0.0358 $mmol_{Ru}.g^{-1}$).

Table S15. Results of recycling experiments performed with $Ru@SILP_{AC}$.

Catalytic Cycle	Surface area ($m^2.g^{-1}$)	Exp. Ru loading [$mmol.g^{-1}$]	$Y_{formate}$ (mmol)	HCOOH/NEt_3 (%)	TON[a]
1	1282	0.08	1.84	11	1043
2	-	0.09	1.89	11	1093
3	-	-	1.84	11	1055
4	-	-	1.66	10	1018
5	-	-	1.84	11	1068
6	-	-	1.71	10	993
7	-	-	1.66	10	930
8	-	-	1.62	9	917
9	-	-	1.53	9	867
10	1106	0.07	1.39	10	965[b]

Reaction Conditions: $Ru@SILP_{AC}$ (50 mg, 1.1 $mmol_{IL}.g^{-1}$, 0.1 $mmol_{Ru}.g^{-1}$ theoretical), 60 bar total pressure with CO_2:H_2 = 1:2, 150 °C, solvent system: NEt_3 (2.32 mL, 16.7 mmol) + H_2O (0.88 mL, 48.8 mmol), total volume: 3.2 mL, NEt_3/H_2O molar ratio = 0.34, time: 1 h; [a]average values of 2-3 experiments based on experimental Ru loadings (0.081 $mmol_{Ru}.g^{-1}$) and estimated surface Ru atoms (0.0358 $mmol_{Ru}.g^{-1}$); [b]based on the amount of catalyst left after run-10.

Table S16. Comparison of Ru@SILP$_{AC}$ with previously reported metal nanoparticle-based catalysts.

Catalyst	Reaction conditions				TON	TOF	Recyclable	Reference
	Temperature (°C)	Pressure (bar)	Solvent System	Time (h)				
Pd/C	40	80 bar CO_2:H_2 = 3:5	ionic liquid (e.g., 1-butyl-3-methylimidazolium acetate	24	594	233.5 mmol·g^{-1}. h^{-1}	5 runs	Ind. Eng. Chem. Res. 2019, 58, 6333−6339
Pd CoO NPs inside the MSN channels	100	20 bar CO_2:H_2 = 1:1	2 mL distilled H_2O containing 2 mmol of $NaHCO_3$	10	4082	1824 h^{-1}	5 runs	ChemCatChem, 2019, 11, 5093 – 5097
Au/SiO_2-Schiff catalyst Schiff-base-modified gold nanocatalyst	90	80 bar CO_2:H_2 = 3:5	15 mmol base, 600 rpm, H_2O/CH_3OH (20:80 vol/vol), 12 h	12	14,470	1206 h^{-1}		Nat. Comm. 2017, 8, 1407
Pd/PIL-2-Tf_2N Pd Nps Supported on Dication Poly(ionic liquid)s	80	20 bar CO_2 No H_2	0.88 M $NaBH_4$ aqueous solution	1		47952 h^{-1}	5 runs	Mol. Catal. 2021, 509, 111644
Pd/ZrO_2 (amorphous)	100	40 bar CO_2:H_2 = 1:1	Aq. $NaHCO_3$			2817 h^{-1}		Mol. Catal. 2019, 475, 110461
PdAg alloy NPs supported on TiO_2	100	20 bar CO_2:H_2 = 1:1	1.0 M aqueous $NaHCO_3$ solution		14 839			J. Am. Chem. Soc. 2018, 140, 8902−8909
PdAg@MIL-101-PEI-50 PdAg Nps supported on MOF	120	80 bar CO_2:H_2 = 1:1	40 mL 1.0 M aqueous $NaHCO_3$	2 h	4968		5 runs	Chem. Eng. J. 2023, 475, 146411
RuFe NPs in ILs	60	30 bar CO_2:H_2 = 1:2	IL (0.27 mmol), D_2O (1.8 mmol), DMSO (36.4 mmol)	17	400	23.5 h^{-1}	-	ACS Catal. 2018, 8, 1621−1627
Sub-nanometer Pd–Mn clusters were encaged within silicalite-1 (S-1) zeolites	80	40 bar CO_2:H_2 = 1:1	2 mL, 1.5 M NaOH solution	-	-	2151 h^{-1}	-	Angew. Chem. Int. Ed. 2020, 59, 20183 – 20191
PdAg Nps supported on phenylamine-functionalized	100	20 bar CO_2:H_2 = 1:1	1.0 M aqueous $NaHCO_3$ solution			3227 mmol h^{-1} g_{Pd}^{-1}	3 runs	ACS Catal. 2018, 8, 2277−2285

mesoporous carbon								
Al_2O_3 supported ruthenium catalyst	80	135 bar CO_2:H_2 = 1:0.6	5 mL NEt_3, 15 mL EtOH	1	91		-	Catal. Today, 2011, 160, 184–190
Ru@SILP (Silica based SILP)	120	90 bar CO_2:H_2 = 1:2	NEt_3 + H_2O + DMSO	20	16 100	1430 h^{-1}	-	Small 2023, *19*, 2206806
Ru@SILP$_{AC}$ (Carbon based SILP)	**150**	**60 bar CO_2:H_2 = 1:2**	**NEt_3 + H_2O**	**20**	**14780**	**3126 h^{-1}**	**9 runs**	**This work**

7. Supplementary figures

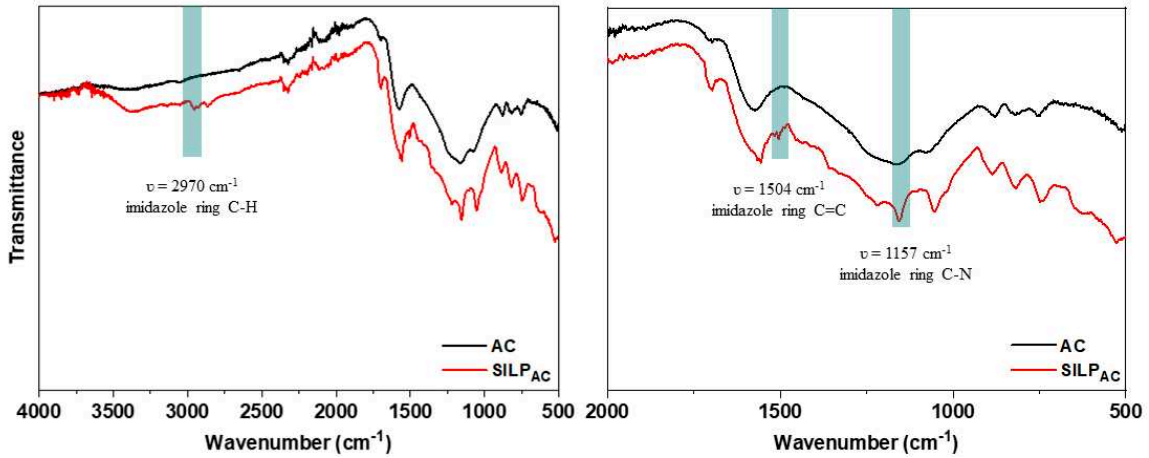

Figure S1. Transmission FT-IR spectra of AC and $SILP_{AC}$, with highlights on the characteristic peaks of IL.

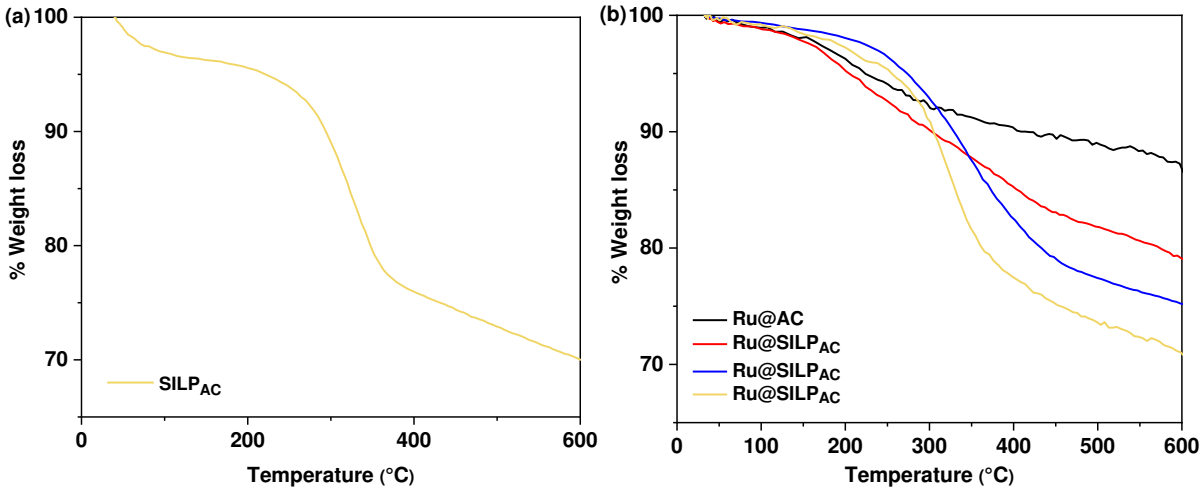

Figure S2. (a) TGA profile of $SILP_{AC}$; (b) TGA profiles of Ru@AC and Ru@$SILP_{AC}$ with varying IL loadings corresponding to 0.5 mmol.g^{-1} (red), 1.1 mmol.g^{-1} (blue), and 2.4 mmol.g^{-1} (yellow).

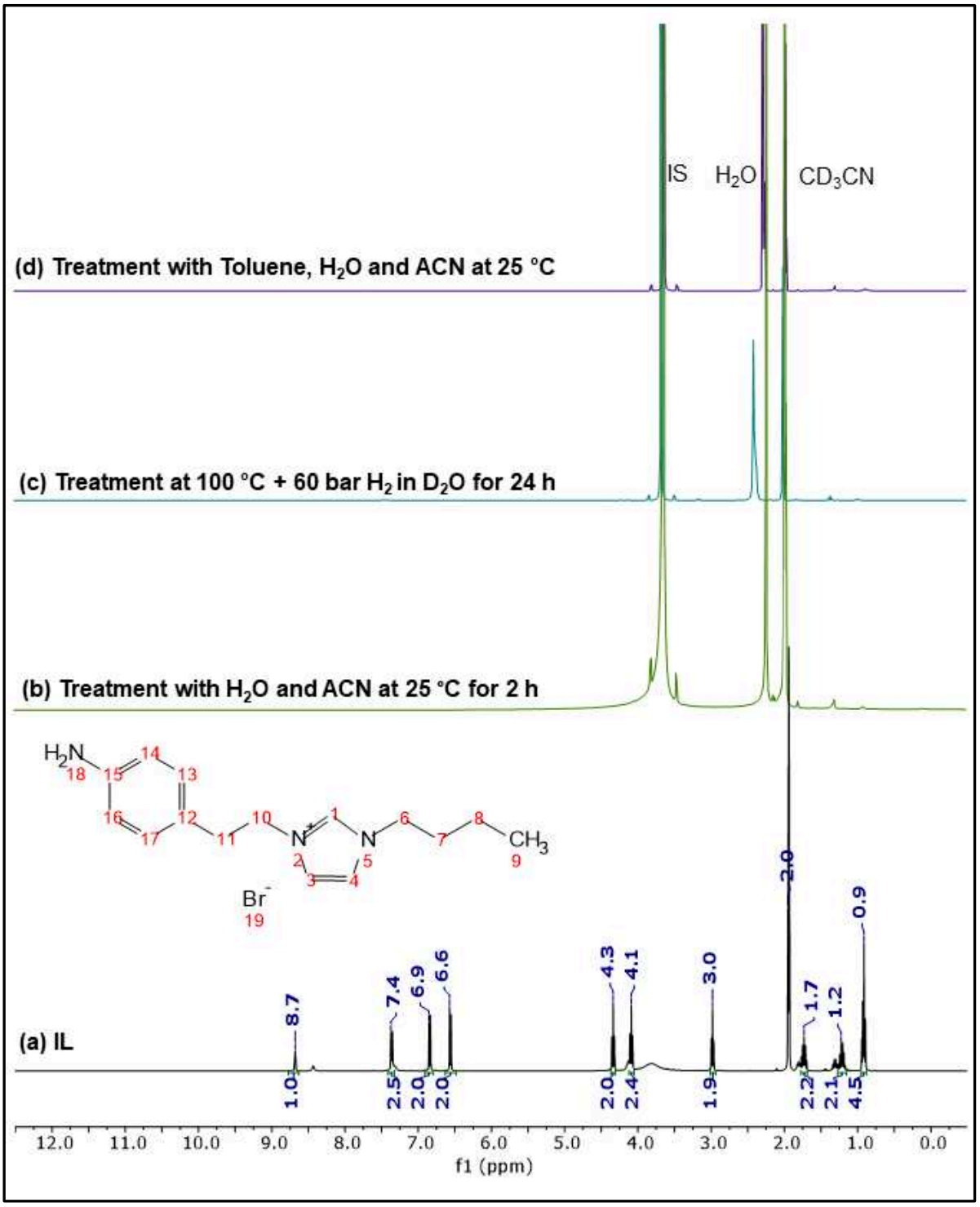

Figure S3. ^{1}H NMR (400 MHz, CD_3CN) of (a) IL; (b) filtrate of $SILP_{AC}$ after treating with H_2O and acetonitrile at 25 °C for 2 h; (c) solution after heating $SILP_{AC}$ at 100 °C + 60 bar H_2 in D_2O for 24 h; (d) filtrate of $SILP_{AC}$ after treating with toluene, H_2O and acetonitrile at 25 °C. Sample preparation is given in section 4.4.6.

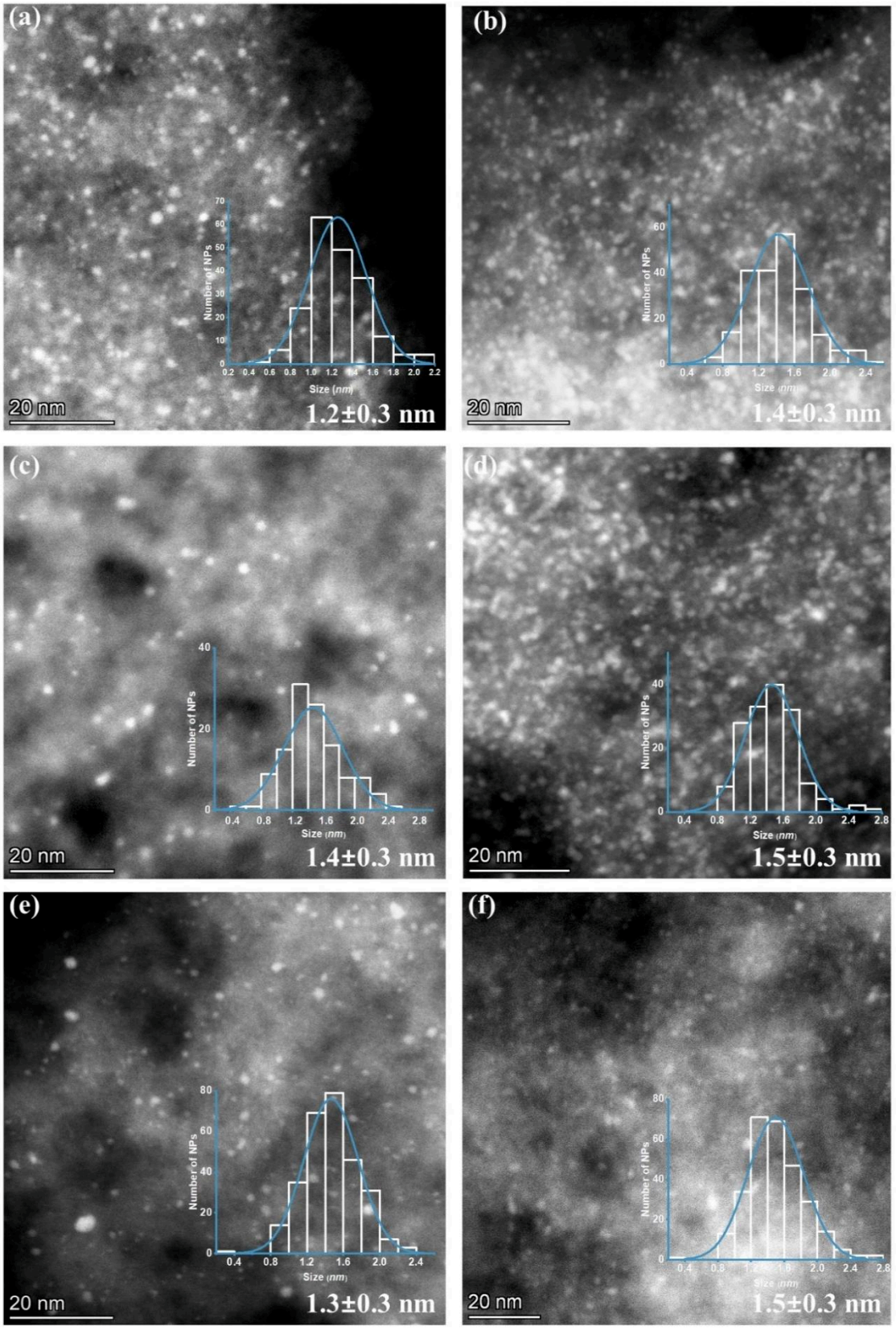

Figure S4. (a) HAADF-STEM image of Ru@AC; (b-f) HAADF-STEM images of Ru@SILP$_{AC}$ with fixed Ru loadings (0.1 mmol$_{Ru}$.g^{-1} theoretical) and varying IL loadings of (b) 0.5 mmol.g^{-1}; (c) 0.8 mmol.g^{-1}; (d) 1.1 mmol.g^{-1}; (e) 1.7 mmol.g^{-1}; (f) 2.4 mmol.g^{-1}.

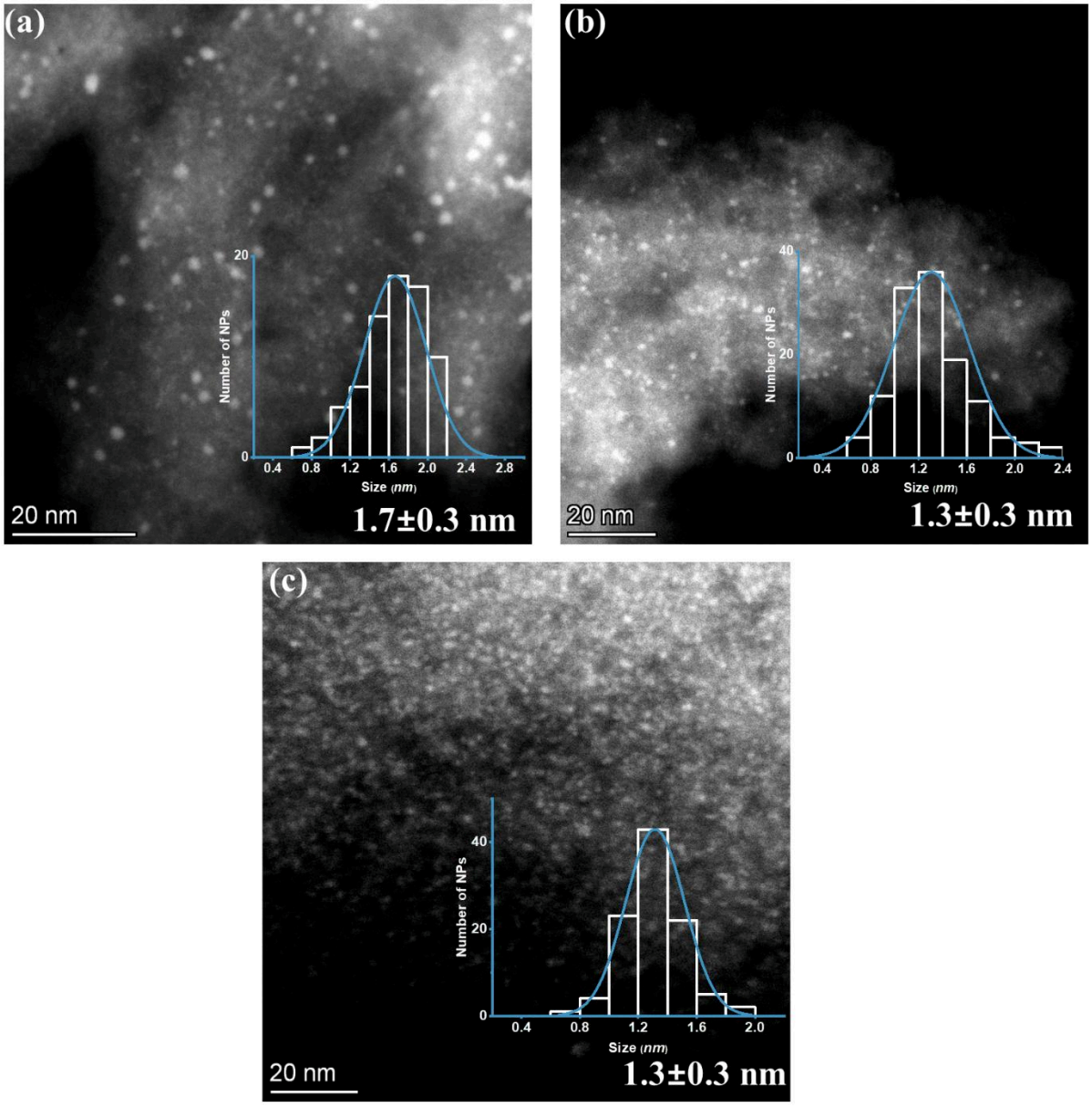

Figure S5. (a-c) HAADF-STEM images of Ru@SILP$_{AC}$ (1.1 mmol$_{IL}$.g^{-1}) with varying theoretical Ru loadings corresponding to (a) 0.025 mmol.g^{-1}; (b) 0.05 mmol.g^{-1}; (c) 0.15 mmol.g^{-1}.

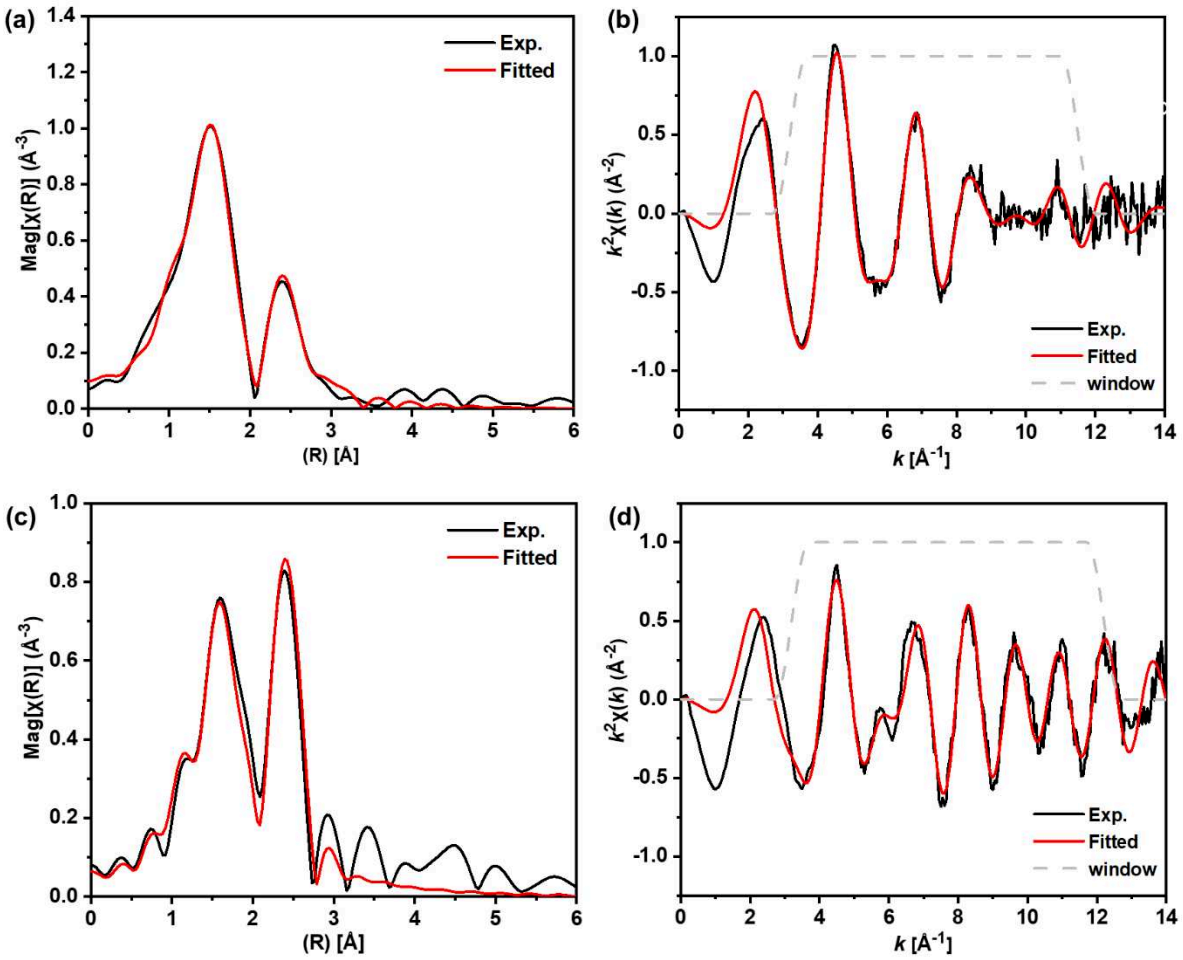

Figure S6. (a, b) Fitting results of k^2-weighted k-space and R-space FT-EXAFS spectra of Ru@AC; (c, d) Fitting results of k^2-weighted k-space and R-space FT-EXAFS spectra of Ru@SILP$_{AC}$.

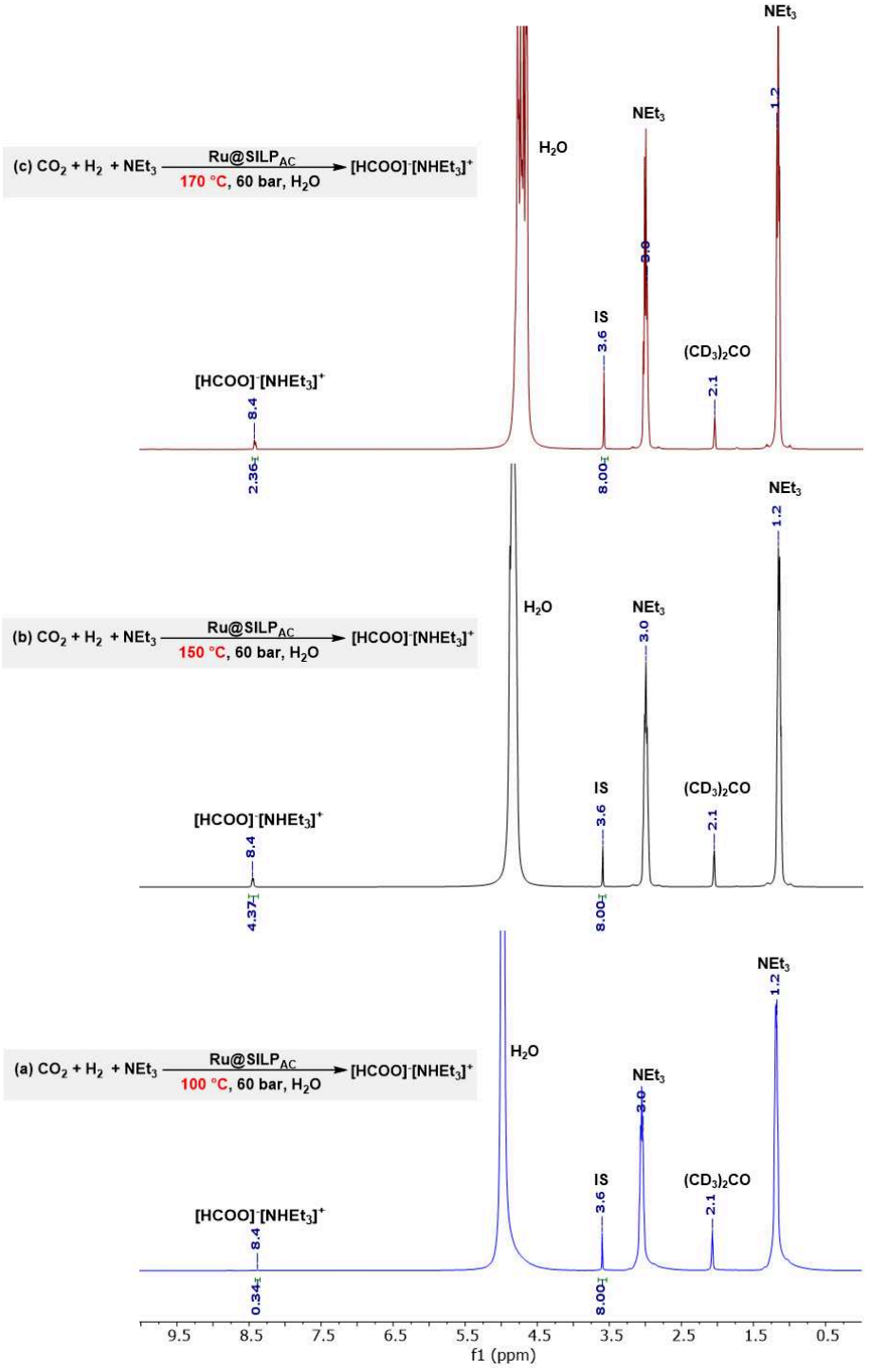

Figure S7. ^{1}H NMR (400 MHz, $(CD_3)_2CO$) spectra for hydrogenation of CO_2 at different temperatures (100 °C, 150 °C and 170 °C). Reaction conditions: Ru@SILP$_{AC}$ (50 mg, 1.1 $mmol_{IL}.g^{-1}$, 0.1 $mmol_{Ru}.g^{-1}$ theoretical, 0.081 mmolRu.g-1 experimental) under 60 bar total pressure with CO_2:H_2 = 1:2 using solvent as NEt_3 (2.32 mL, 16.7 mmol) + H_2O (0.88 mL, 48.8 mmol), total volume: 3.2 mL, NEt_3/H_2O molar ratio = 0.34, time: 1 h. Product quantification was obtained using 1,4-dioxane as a standard (0.45 mmol).

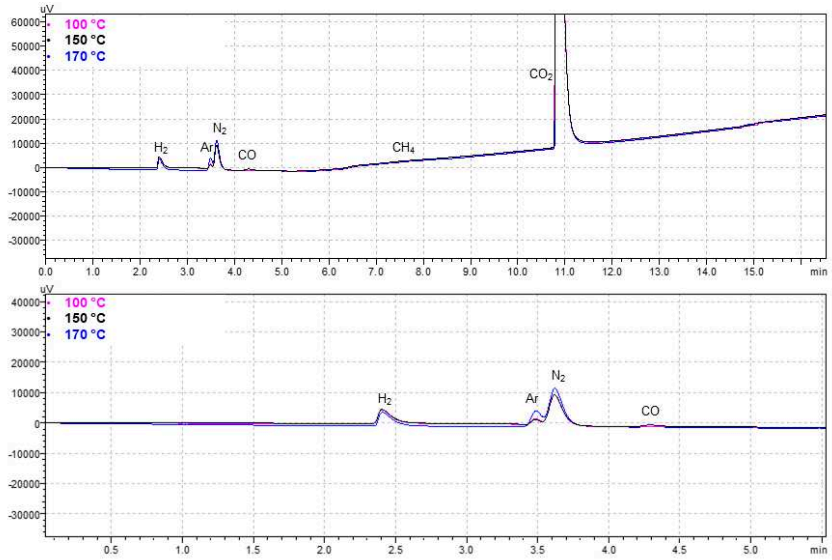

Ret. Time	Peaks	Norm. Conc.		
		100 °C	150 °C	170 °C
2.40	H_2	65.22	67.28	66.55
3.48	Ar	0.192	0.52	0.157
4.29	CO	--	0.038	0.079
7.5	CH_4	--	--	--
10.8	CO_2	34.58	32.16	33.22

Figure S8. GC-TCD spectra and results for hydrogenation of CO_2 at different temperatures (100 °C, 150 °C, and 170 °C). Reaction Conditions: Ru@SILP$_{AC}$ (50 mg, 1.1 $mmol_{IL}.g^{-1}$, 0.1 $mmol_{Ru}.g^{-1}$ theoretical, 0.081 $mmol_{Ru}.g^{-1}$ experimental) under 60 bar total pressure with CO_2:H_2 = 1:2 using solvent as NEt_3 (2.32 mL, 16.7 mmol) + H_2O (0.88 mL, 48.8 mmol), total volume: 3.2 mL, NEt_3/H_2O molar ratio = 0.34, time: 1 h.

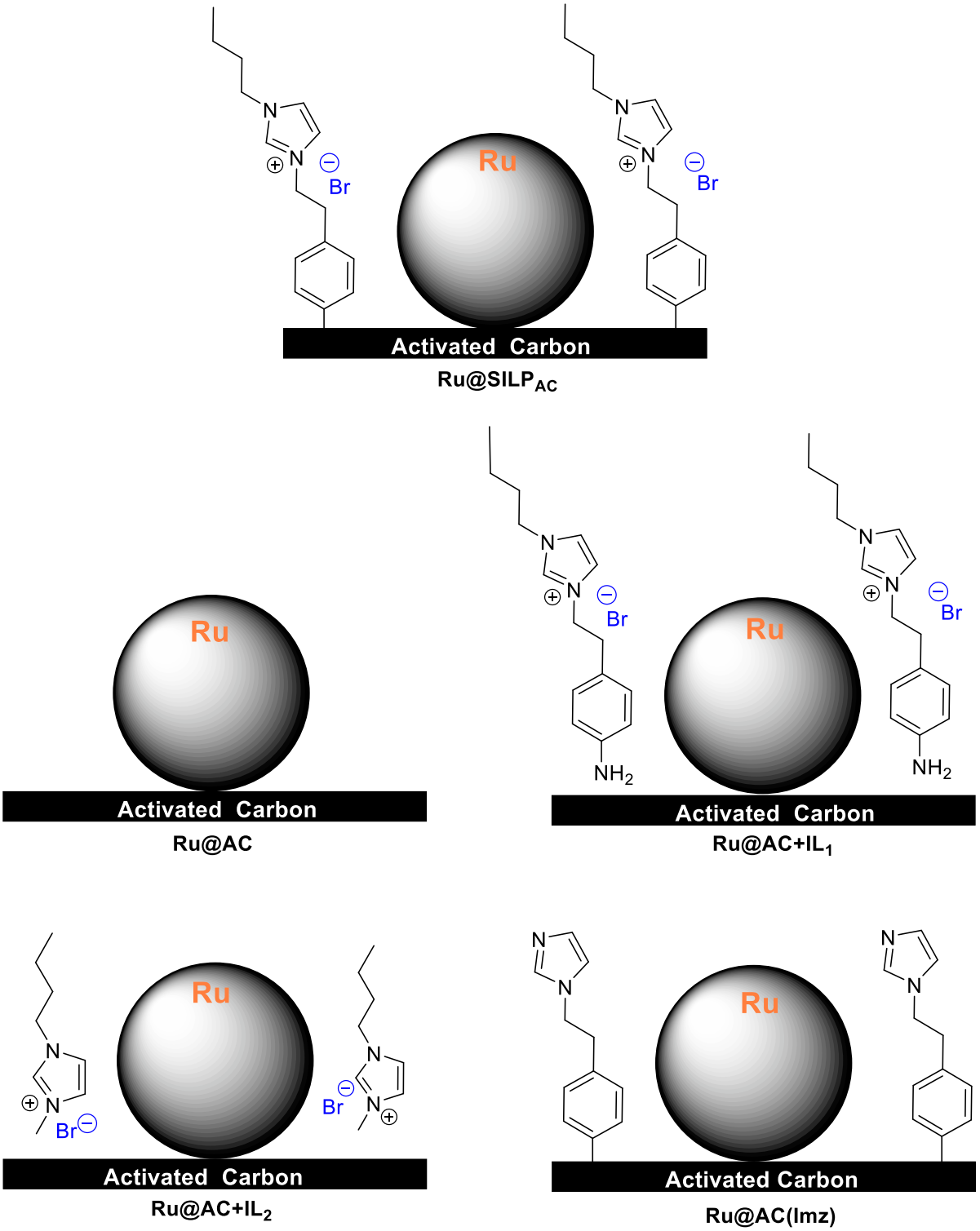

Figure S9. Illustration of Ru NPs immobilized on different types of MMS supports.

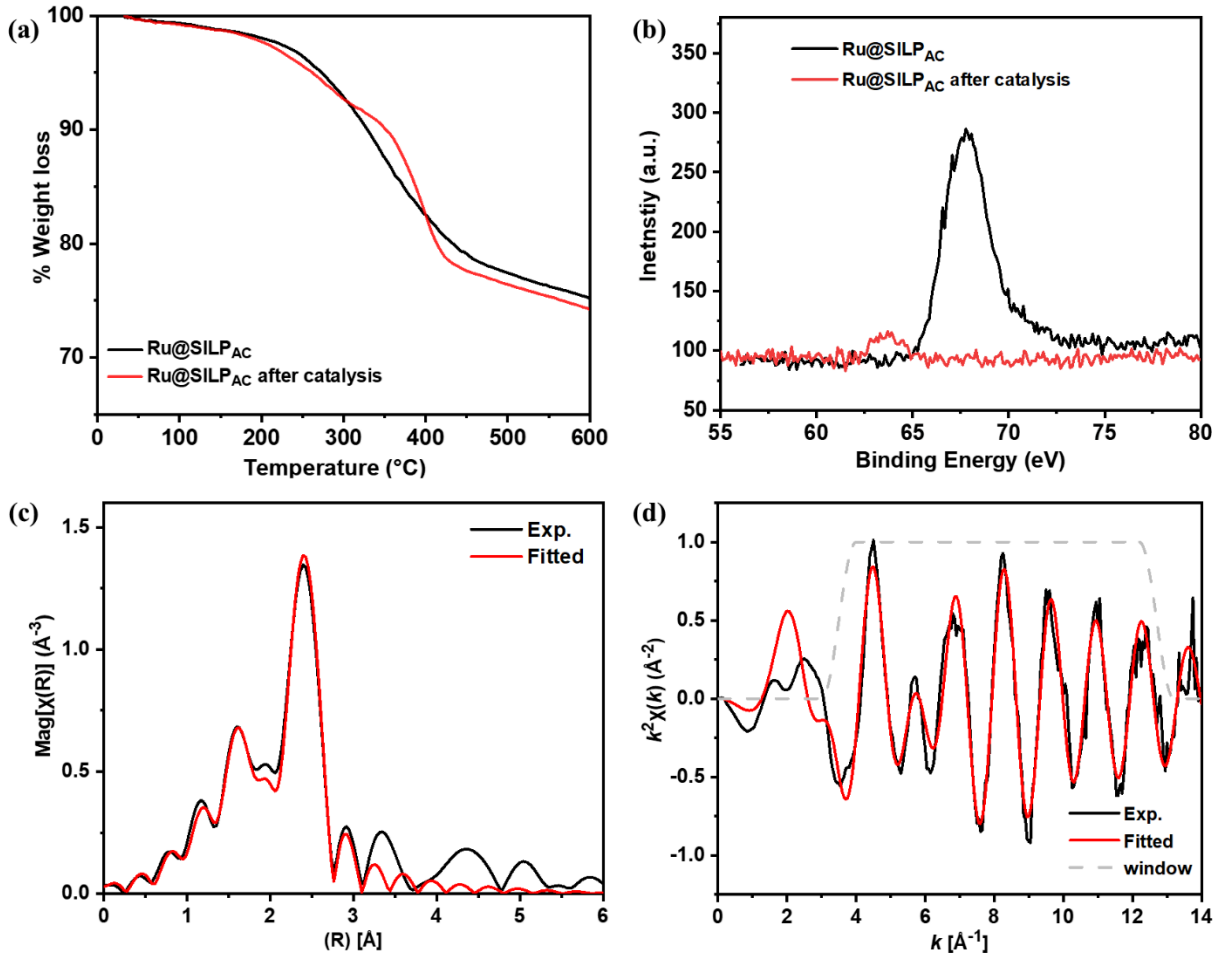

Figure S10. (a) TGA curves of Ru@SILP$_{AC}$ of fresh catalyst and after Run-10; (b) Br 3d XPS spectra of Ru@SILP$_{AC}$ before and after Run-1; (c) EXAFS spectra and best fit in R-space of Ru@SILP$_{AC}$ after Run-1; (d) EXAFS spectra and best fit in k-space of Ru@SILP$_{AC}$ after Run-1. Reaction conditions: Ru@SILP$_{AC}$ (50 mg, 1.1 mmol$_{IL}$.g^{-1}, 0.1 mmol$_{Ru}$.g^{-1} theoretical, 0.081 mmol$_{Ru}$.g^{-1} experimental), 60 bar total pressure with CO_2:H_2 = 1:2 at 150 °C using solvent as NEt_3 (2.32 mL, 16.7 mmol) + H_2O (0.88 mL, 48.8 mmol), total volume: 3.2 mL, NEt_3/H_2O molar ratio = 0.34, time: 1 h.

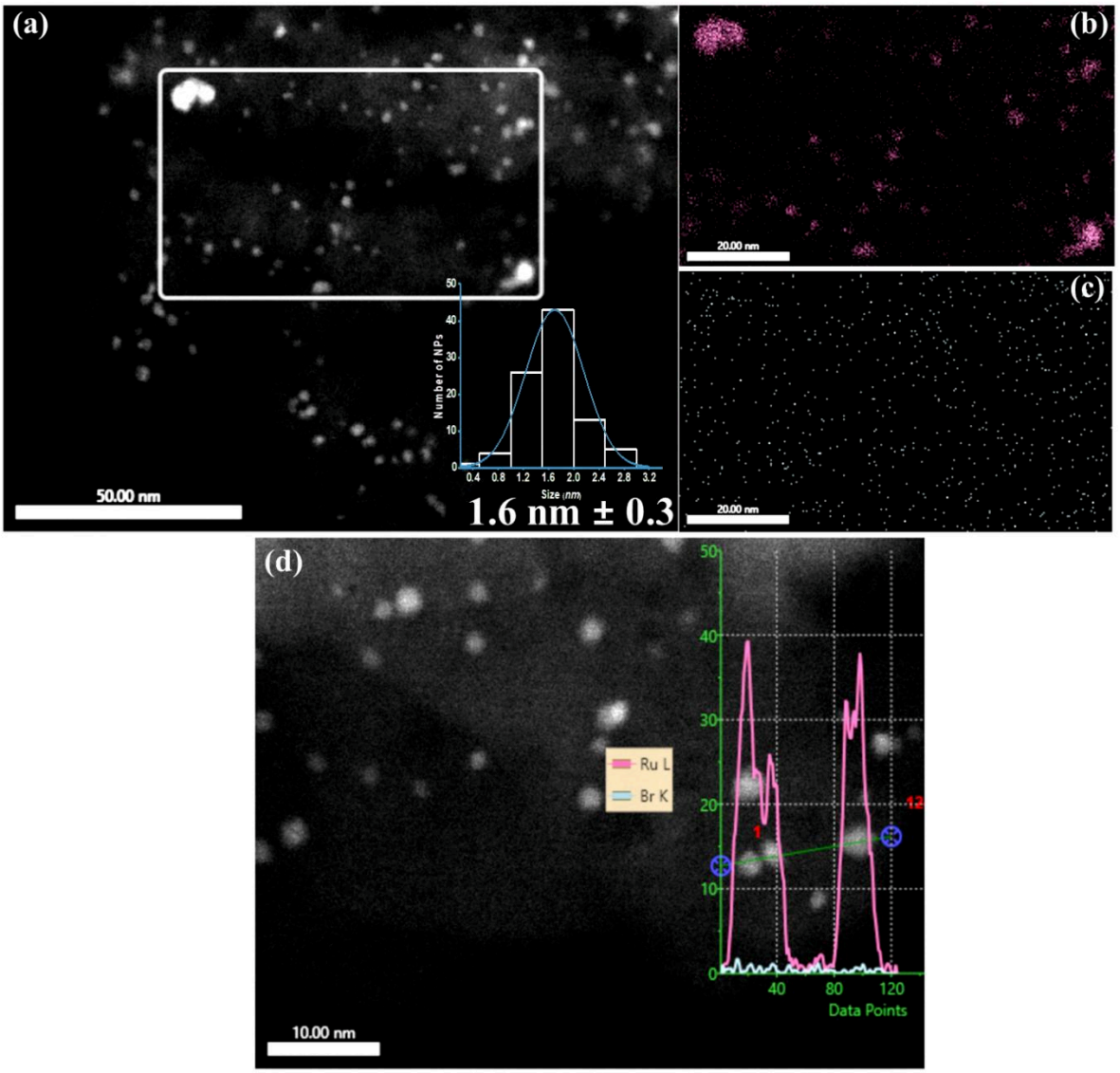

Figure S11. (a) HAADF-STEM image of Ru@SILP$_{AC}$ after 10 cycles; (b-c) HAADF-STEM-EDX elemental mapping images of (b) Ru Lα and (c) Br Kα; (d) HAADF-STEM- elemental distribution counts of Ru L and Br K for Ru@SILP$_{AC}$ after 10 cycles. Reaction conditions: Ru@SILP$_{AC}$ (50 mg, 1.1 $mmol_{IL}.g^{-1}$, 0.1 $mmol_{Ru}.g^{-1}$ theoretical, 0.081 $mmol_{Ru}.g^{-1}$ experimental), 60 bar total pressure with CO_2:H_2 = 1:2, solvent system: NEt_3 (2.32 mL, 16.7 mmol) + H_2O (0.88 mL, 48.8 mmol), total volume: 3.2 mL, NEt_3/H_2O molar ratio = 0.34, time: 1 h.

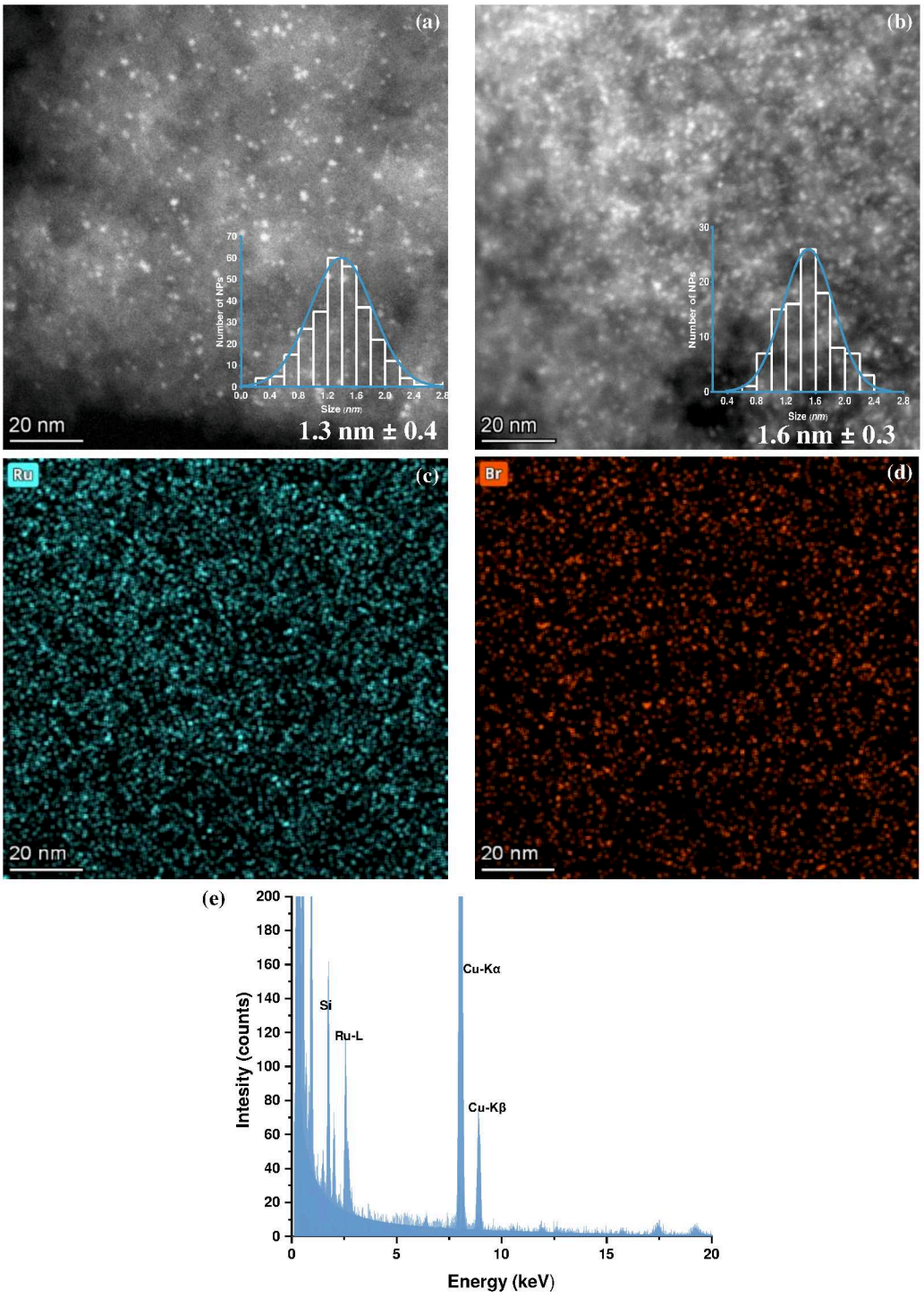

Figure S12. (a) HAADF-STEM image of Ru@AC after Run-1; (b) HAADF-STEM image of Ru@SILP$_{AC}$ after Run-1; (c-d) HAADF-STEM-EDX elemental mapping of (c) Ru Lα and (d) Br Kα for Ru@SILP$_{AC}$; (e) EDX spectra (sum spectra) of Ru@SILP$_{AC}$ after Run-1; Reaction conditions: Ru@SILP$_{AC}$ (50 mg, 1.1 mmol$_{IL}$.g^{-1}, 0.1 mmol$_{Ru}$.g^{-1} theoretical, 0.081 mmol$_{Ru}$.g^{-1} experimental), 60 bar total pressure with CO_2:H_2 = 1:2, solvent system: NEt_3 (2.32 mL, 16.7 mmol) + H_2O (0.88 mL, 48.8 mmol), total volume: 3.2 mL, NEt_3/H_2O molar ratio = 0.34, time: 1 h.

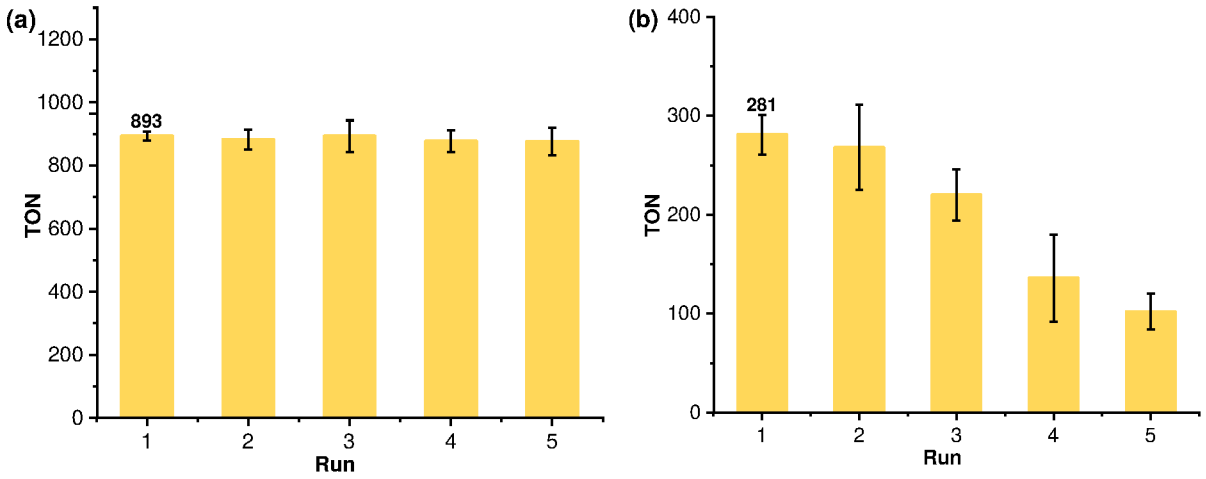

Figure S13. Recycling of (a) Ru@SILP$_{AC}$ (50 mg, 1.1 mmol$_{IL}$.g^{-1}, 0.1 mmol$_{Ru}$.g^{-1} theoretical); (b) Ru@AC (50 mg, 0.1 mmol$_{Ru}$.g^{-1} theoretical). Reaction conditions: 60 bar total pressure with CO_2:H_2 = 1:2, 100 °C, NEt_3 (3.95 mmol, 0.55 mL) + H_2O (41 mmol, 0.75 mL), 20 h. TON has been estimated based on experimental Ru loadings (Ru@AC: 0.085 mmol$_{Ru}$.g^{-1}; Ru@SILP$_{AC}$: 0.081 mmol$_{Ru}$.g^{-1}) and estimated surface Ru atoms (Ru@AC: 0.044 mmol$_{Ru}$.g^{-1}; Ru@SILP$_{AC}$: 0.0358 mmol$_{Ru}$.g^{-1}). Data points are average values of 2-3 experiments, and error bars represent standard deviations.

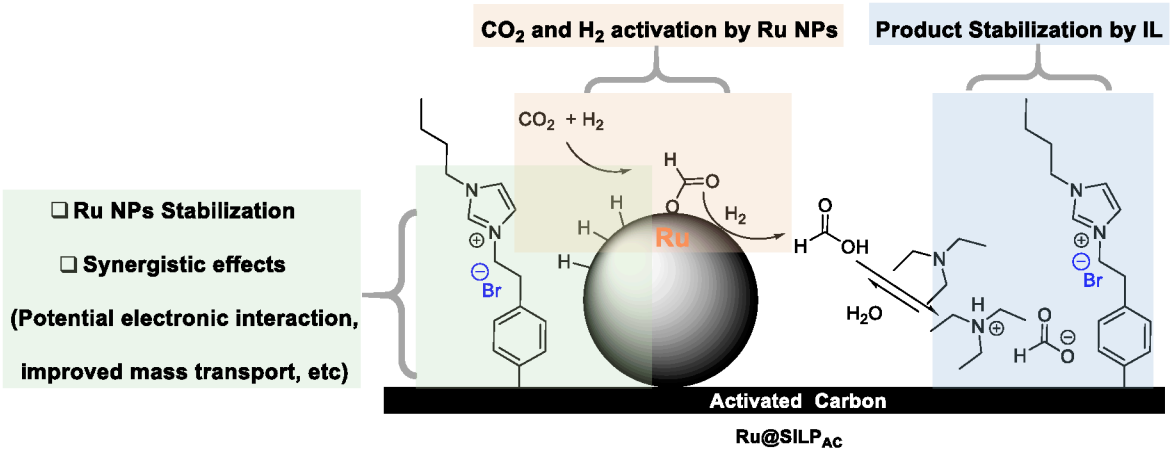

Figure S14. Illustration of the hydrogenation of CO_2 at the surface of Ru@SILP$_{AC}$, including the key role(s) of the different catalyst components.

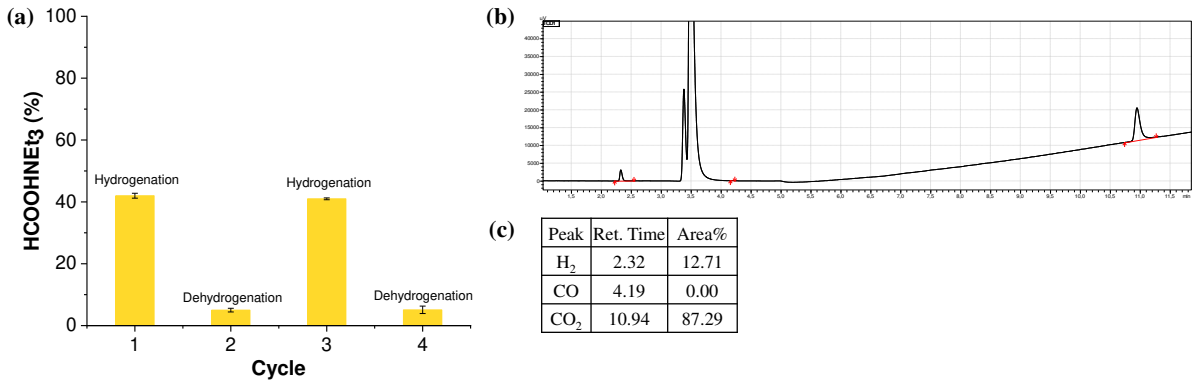

Peak	Ret. Time	Area%
H_2	2.32	12.71
CO	4.19	0.00
CO_2	10.94	87.29

Figure S15. (a) Reversible hydrogenation/dehydrogenation using Ru@SILP$_{AC}$; (b) GC-TCD spectra after cycle 1; (c) Table for peak areas of chromatogram. Reaction conditions for hydrogenation: Ru@SILP$_{AC}$ (50 mg, 1.1 mmol$_{IL}$.g^{-1}, 0.1 mmol$_{Ru}$.g^{-1} theoretical), 60 bar total pressure with CO_2:H_2 = 1:2, 100 °C, NEt_3 (3.95 mmol, 0.55 mL) + H_2O (41 mmol, 0.75 mL), 20 h; Reaction conditions for dehydrogenation: Recycled Ru@SILP$_{AC}$, 100 °C, using reaction mixture obtained after hydrogenation, 20 h. Data points are average values of 2-3 experiments, and error bars represent standard deviations.

8. NMR Spectra

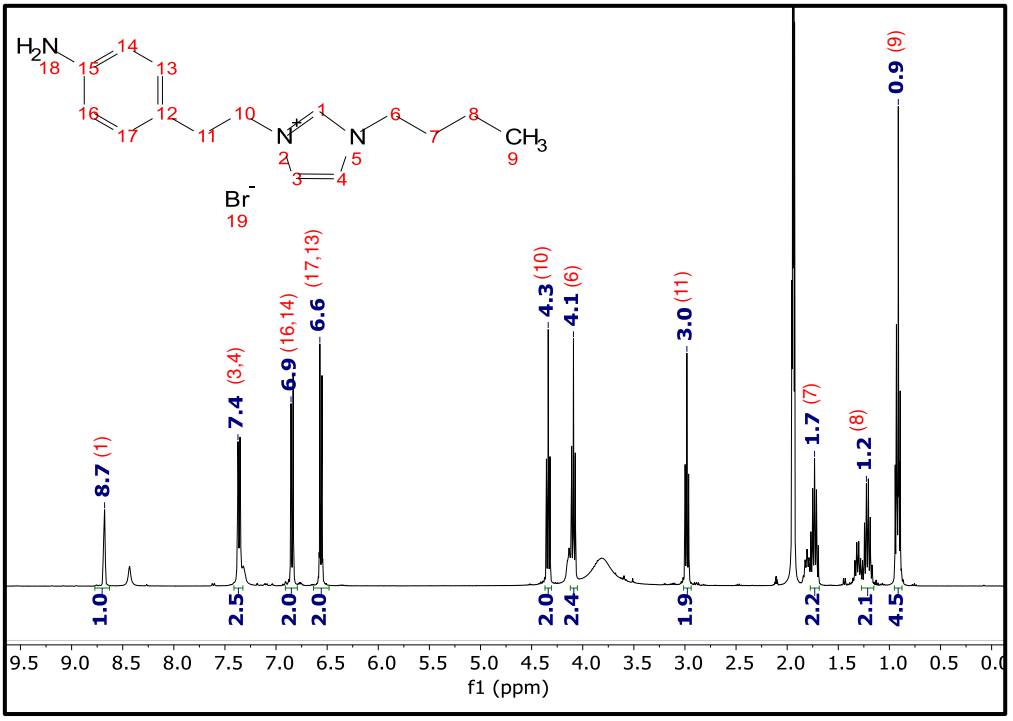

Figure S16. ^{1}H NMR (400 MHz, CD_3CN) spectrum of [3-(4-aminophenethyl)-1-butyl-1H-imidazol-3-ium]Br.

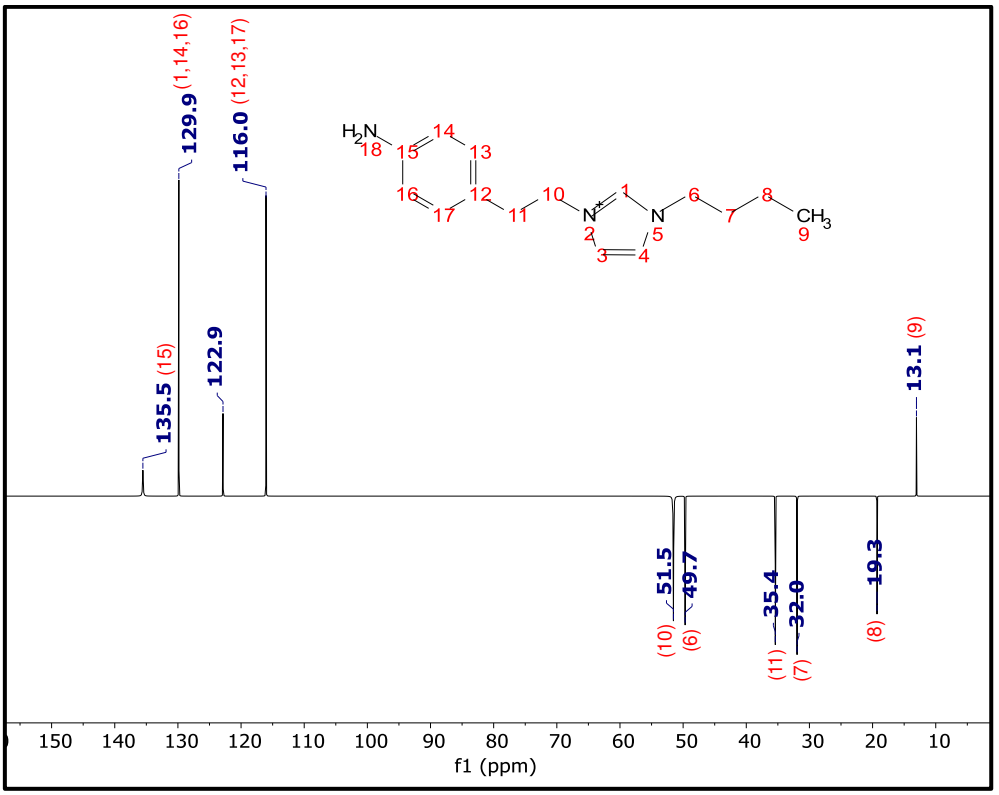

Figure S17. ^{13}C NMR (DEPT) (100.6 MHz, CD_3CN) spectrum of [3-(4-aminophenethyl)-1-butyl-1H-imidazol-3-ium]Br.

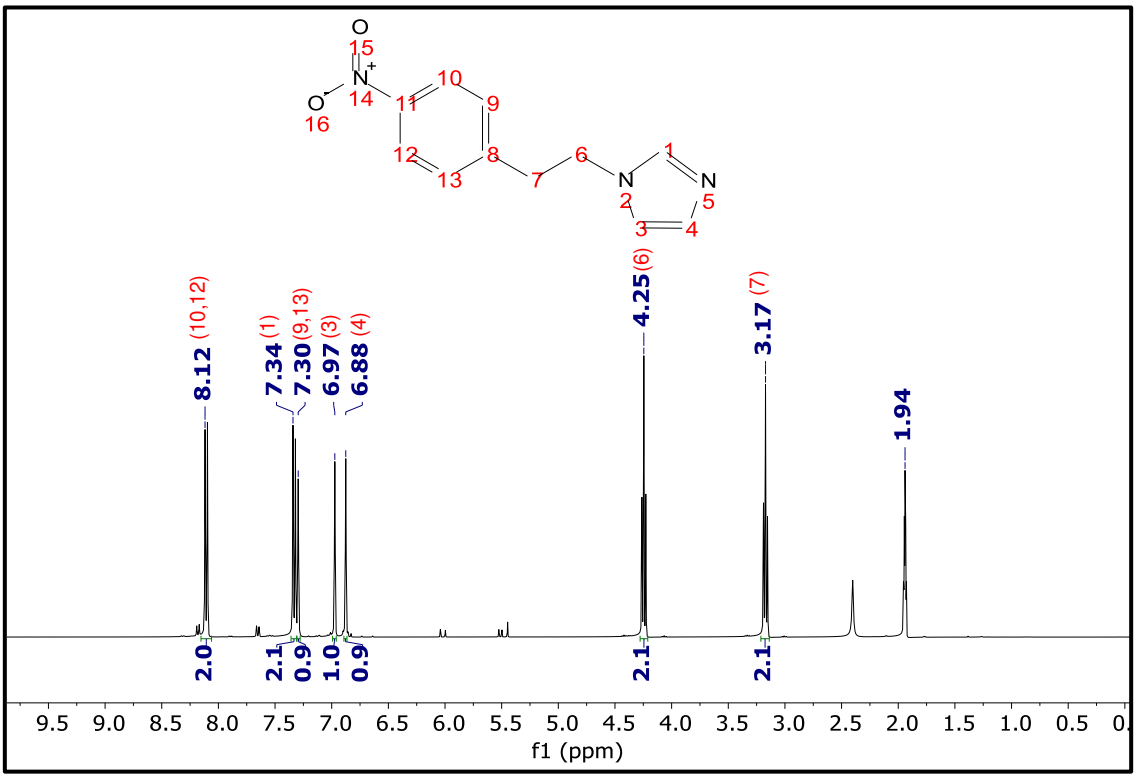

Figure S18. ^{1}H NMR (400 MHz, CD_3CN) spectrum of 1-(4-nitrophenethyl)-1H-imidazole.

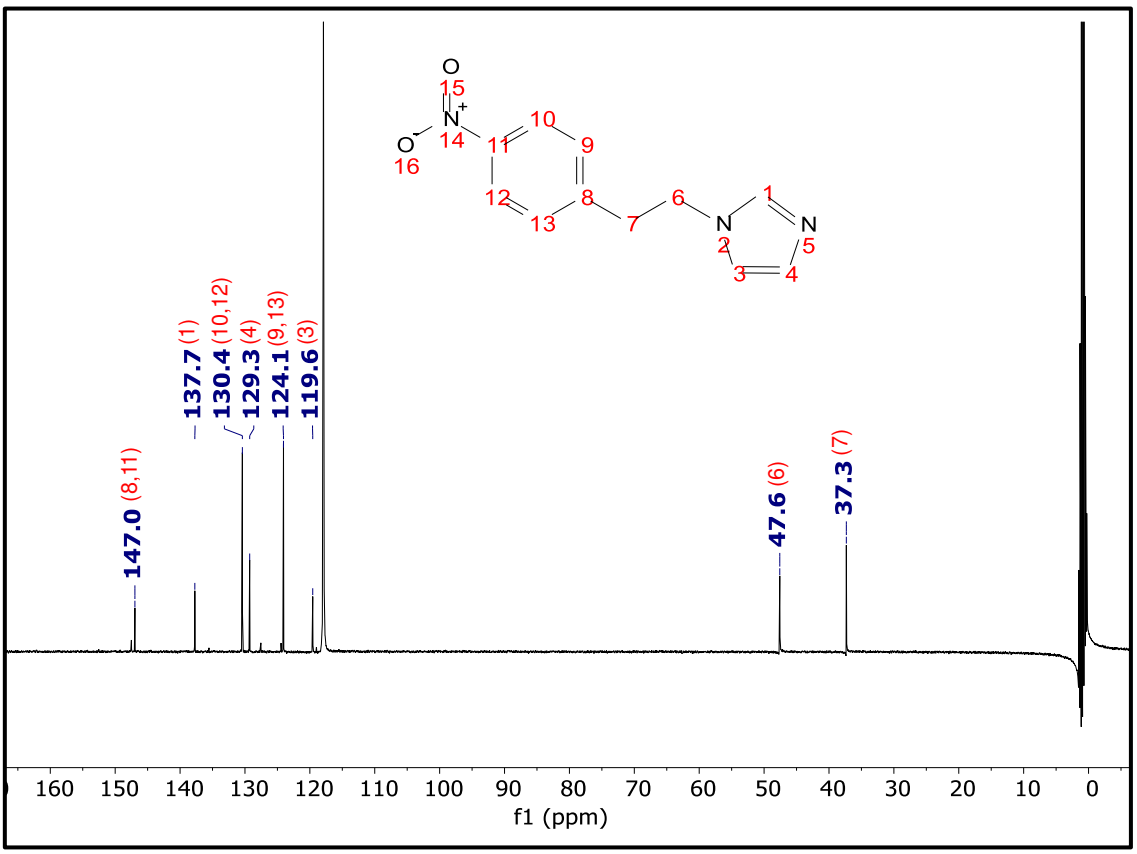

Figure S19. ^{13}C NMR (101 MHz, CD_3CN) spectrum of 1-(4-nitrophenethyl)-1H-imidazole.

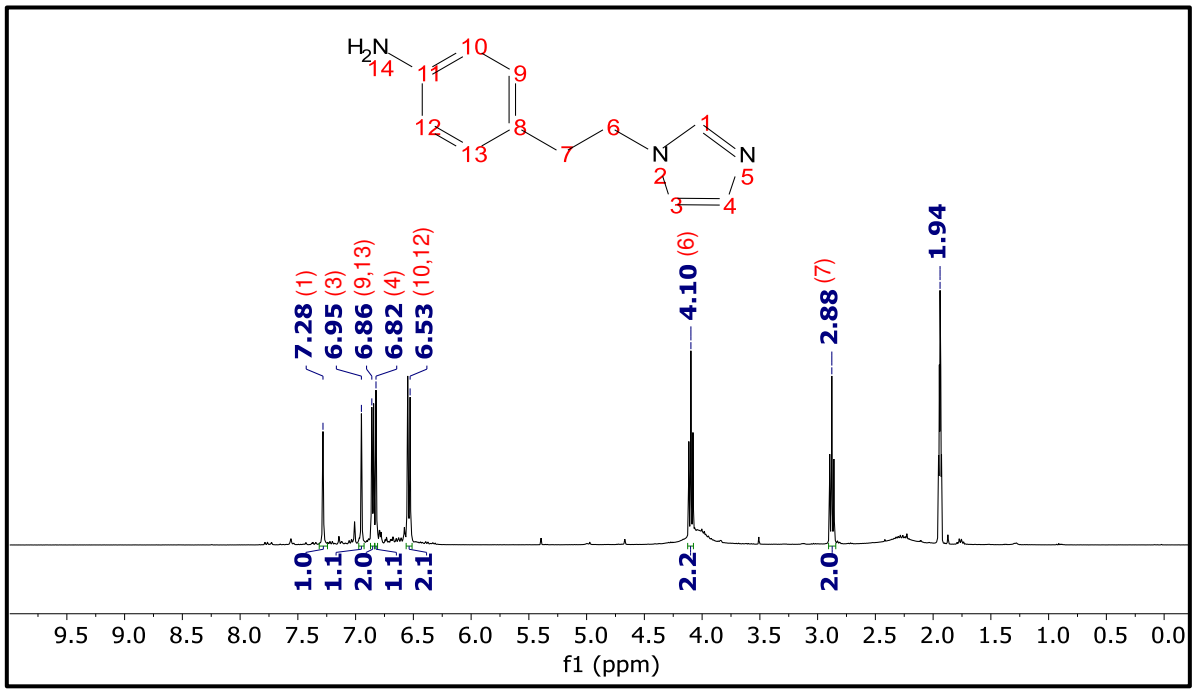

Figure S20. ^{1}H NMR (400 MHz, CD_3CN) spectrum of 4-(2-(1H-imidazol-1-yl)ethyl)aniline (Imz).

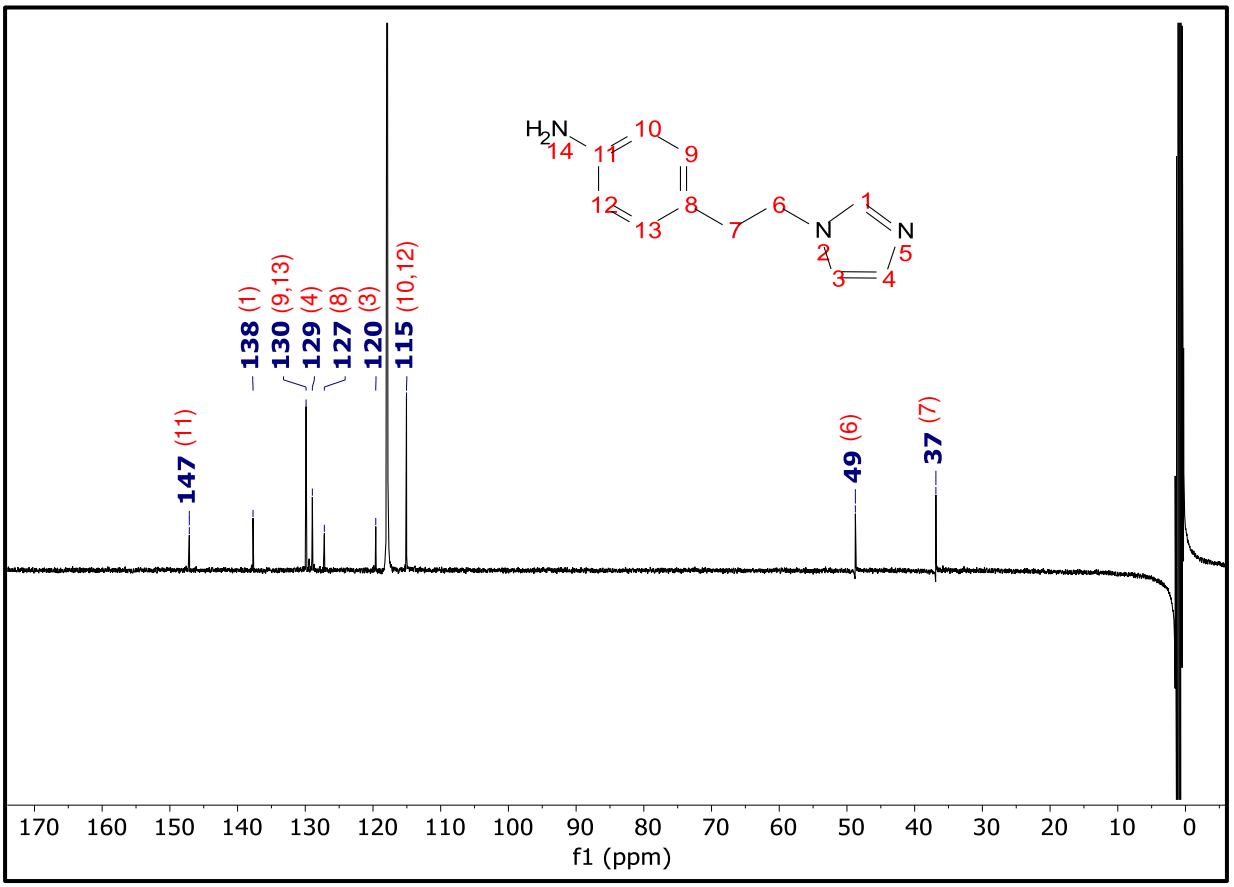

Figure S21. ^{13}C NMR (101 MHz, CD_3CN) spectrum of 4-(2-(1H-imidazol-1-yl)ethyl)aniline (Imz).

9. References

(1) Fairley, N.; Fernandez, V.; Richard-Plouet, M.; Guillot-Deudon, C.; Walton, J.; Smith, E.; Flahaut, D.; Greiner, M.; Biesinger, M.; Tougaard, S.; et al. Systematic and collaborative approach to problem solving using X-ray photoelectron spectroscopy. *Appl. Surf. Sci. Adv.* **2021**, *5,* 100112.
(2) Welter, E.; Chernikov, R.; Herrmann, M.; Nemausat, R. A beamline for bulk sample x-ray absorption spectroscopy at the high brilliance storage ring PETRA III. *AIP Conference Proceedings* **2019**, *2054*.
(3) Ravel, B.; Newville, M. ATHENA, ARTEMIS, HEPHAESTUS: data analysis for X-ray absorption spectroscopy using IFEFFIT. *J. Synchrotron Radiat.* **2005**, *12*, 537-541.
(4) Levin, N.; Goclik, L.; Walschus, H.; Antil, N.; Bordet, A.; Leitner, W. Decarboxylation and Tandem Reduction/Decarboxylation Pathways to Substituted Phenols from Aromatic Carboxylic Acids Using Bimetallic Nanoparticles on Supported Ionic Liquid Phases as Multifunctional Catalysts. *J. Am. Chem. Soc.* **2023**, *145,* 22845-22854.
(5) Goclik, L.; Walschus, H.; Bordet, A.; Leitner, W. Selective hydrodeoxygenation of acetophenone derivatives using a $Fe_{25}Ru_{75}$@SILP catalyst: a practical approach to the synthesis of alkyl phenols and anilines. *Green Chem.* **2022**, *24,* 2937-2945.
(6) Louis Anandaraj, S. J.; Kang, L.; DeBeer, S.; Bordet, A.; Leitner, W. Catalytic Hydrogenation of CO2 to Formate Using Ruthenium Nanoparticles Immobilized on Supported Ionic Liquid Phases. *Small* **2023**, *19*, 2206806.
(7) Fang, M.; Wang, K.; Lu, H.; Yang, Y.; Nutt, S. Covalent polymer functionalization of graphene nanosheets and mechanical properties of composites. *J. Mater. Chem.* **2009**, *19,* 7098-7105.
(8) Bahr, J. L.; Tour, J. M. Highly Functionalized Carbon Nanotubes Using in Situ Generated Diazonium Compounds. *Chem. Mater.* **2001**, *13*, 3823-3824.